Determinants within the Turret and Pore-Loop Domains of KCNQ3 K^+ Channels Governing Functional Activity

Oleg Zaika, Ciria C. Hernandez, Manjot Bal, Gleb P. Tolstykh, and Mark S. Shapiro
Department of Physiology, University of Texas Health Science Center at San Antonio, San Antonio, Texas

ABSTRACT KCNQ1–5 (Kv7.1–7.5) subunits assemble to form a variety of functional K^+ channels in the nervous system, heart, and epithelia. KCNQ1 and KCNQ4 homomers and KCNQ2/3 heteromers yield large currents, whereas KCNQ2 and KCNQ3 homomers yield small currents. Since the unitary conductance of KCNQ3 is five- to 10-fold greater than that of KCNQ4 or KCNQ1, these differences are even more striking. To test for differential membrane protein expression, we performed biotinylation and total internal reflection fluorescence imaging assays; however, both revealed only small differences among the channels, leading us to investigate other mechanisms at work. We probed the molecular determinants governing macroscopic current amplitudes, with focus on the turret and pore-loop domains of KCNQ1 and KCNQ3. Elimination of the putative N289 glycosylation site in KCNQ1 reduced current density by ~56%. A chimera consisting of KCNQ3 with the turret domain (TD) of KCNQ1 increased current density by about threefold. Replacement of the proximal half of the TD in KCNQ3 with that of KCNQ1 increased current density by fivefold. A triple chimera containing the TD of KCNQ1 and the carboxy terminus of KCNQ4 yielded current density 10- or sixfold larger than wild-type KCNQ3 or KCNQ1, respectively, suggesting that the effects on current amplitudes of the TD and the carboxy-terminus are additive. Critical was the role of the intracellular TEA^+-binding site. The KCNQ3 (A315T) swap increased current density by 10-fold, and the converse KCNQ1 (T311A) swap reduced it by 10-fold. KCNQ3 (A315S) also yielded greatly increased current amplitudes, whereas currents from mutant A315V channels were very small. The KCNQ3 (A315T) mutation increased the sensitivity of the channels to external Ba^{2+} block by eight- to 28-fold, consistent with this mutation altering the structure of the selectivity filter. To investigate a structural hypothesis for the effects of these mutations, we performed homology modeling of the pore region of wild-type and mutant KCNQ3 channels, using KvAP as a template. The modeling suggests a critical stabilizing interaction between the pore helix and the selectivity filter that is absent in wild-type KCNQ3 and the A315V mutant, but present in the A315T and A315S mutants. We conclude that KCNQ3 homomers are well expressed at the plasma membrane, but that most wild-type channels are functionally silent, with rearrangements of the pore-loop architecture induced by the presence of a hydroxyl-containing residue at the 315 position "unlocking" the channels into a conductive conformation.

INTRODUCTION

A number of different critical K^+ currents are made by the family of KCNQ (Kv7) K^+ channels in the heart, ear, nerves, and epithelia (1). The activity of these channels is highly modulated by a number of intracellular signaling molecules, including phosphatidylinositol 4,5-bisphosphate (PIP_2), Ca^{2+}/calmodulin, and protein kinases (2,3). In neurons, most channels are heteromers of KCNQ2 and KCNQ3, although KCNQ5-containing channels and KCNQ2 and KCNQ3 homomers are also present (4–12). In the inner ear, KCNQ4 forms homomeric channels critical to K^+ transport (13,14), and in the heart, ear, and epithelia, KCNQ1 forms heteromeric channels with KCNE β-subunits (3). Therefore, the variety of possible KCNQ assemblies provides for a rich diversity of available expression patterns of these channels.

However, heterologous-expression studies have shown that the various KCNQ combinations yield sharply divergent macroscopic amplitudes in both oocytes and mammalian cells. Thus, expression of KCNQ2 and KCNQ3 individually yields only small whole-cell currents, whereas their coexpression yields heteromeric currents 10-fold larger (4,15–19). Likewise, the amplitudes of the different homomeric channels are strikingly different when heterologously expressed, with KCNQ4 and KCNQ1 homomers yielding much larger currents than KCNQ2 or KCNQ3 (14,18–21). The wide differences in current amplitudes between the channel types are even more striking if one considers their single-channel properties. KCNQ2 and KCNQ3 have unitary conductances three to five times greater than those of KCNQ4 or KCNQ1 (22–24), and the maximal open probability of KCNQ3 is 10-fold greater than that of KCNQ4 (25).

Three disparate regions of the channels have been implicated in governing macroscopic current amplitudes. The first is the subunit-interaction domain (SID), or A-domain, within the distal carboxy terminus of the channels (26), in which two coiled-coiled domains are required for homomeric and heteromeric assembly and functional expression (19), likely via salt-bridge interactions between the coils (27,28). The second is in the pore region, including the ''turret'', whose deter-

Submitted May 20, 2008, and accepted for publication July 28, 2008.

Address reprint requests to Mark S. Shapiro, PhD, Department of Physiology, MS 7756, University of Texas Health Science Center at San Antonio, 7703 Floyd Curl Drive, San Antonio, TX 78229. Tel.: 210-567-4328; Fax: 210-567-4410; E-mail: shapirom@uthscsa.edu.

Editor: Eduardo Perozo.

0006-3495/08/12/5121/17 $2.00

doi: 10.1529/biophysj.108.137604

minants are further studied here. The third is the amino-terminus, which has been suggested to play a strong role in controlling the activity of channels expressed in the membrane (15). Although several articles have concluded that the differential currents produced by homomeric and heteromeric channels, or among the different homomers, arise from parallel differences in expression of the channels to the membrane (19,20,26,29), other work did not find such a correlation between surface expression and macroscopic currents (15). For KCNQ2 homomers, we have previously shown that their small macroscopic currents are due to their low apparent affinity for PIP_2; thus, an increase in tonic PIP_2 abundance in the membrane increases the KCNQ2 currents by almost 10-fold, to the level typical of KCNQ2/3 heteromers (25).

We set out to systematically probe the issue of whether the highly disparate macroscopic currents arise from a differential surface expression of the channels, with particular focus on KCNQ3, whose very low current amplitudes are particularly discordant with their unitary properties. We performed several assays of membrane expression in mammalian Chinese hamster ovary (CHO) cells, including biotinylation assays and total internal reflection fluorescence (TIRF) microscopy. Neither assay reported large differences in surface expression of the order that would account for the sharp differences in macroscopic currents. We then investigated the molecular determinants within KCNQ3 responsible for its small current, focusing on the turret and pore loop domains that were identified as a major locus for such control (15,20). Finally, we performed homology modeling to try to understand how the architecture of the wild-type and mutant channels in this region results in nonfunctional or fully active channels. We conclude that KCNQ3 homomers are well expressed at the membrane, but that most of them are normally dormant and do not produce measurable currents.

MATERIALS AND METHODS

cDNA constructs

Human KCNQ1–5 (Genbank accession numbers AAC51781, AF110020, AAC96101, AF105202, and AF249278, respectively) were kindly given to us by Michael Sanguinetti (KCNQ1, University of Utah, Salt Lake City, UT), David McKinnon (KCNQ2, SUNY, Stony Brook, NY), Thomas Jentsch (KCNQ3, KCNQ4, Zentrum fur Molekulare Neurobiologie, Hamburg, Germany), and Klaus Steinmeyer (KCNQ5, Sanofi-Aventis Pharmaceuticals, Frankfurt-am-Main, Germany). Plasmids were subcloned into pcDNA3.1, pECFP-N1, or pEYFP-N1 vectors (Clontech, Mountainview, CA) using standard techniques. Myc-tagged KCNQ1–4 channels were generated by subcloning each channel in frame into cytomegalovirus-myc (pCMV) vector (Clontech) behind the myc epitope.

Cell culture and transfections

CHO cells were grown in 100-mm tissue-culture dishes (Falcon, Franklin Lakes, NJ) in DMEM medium with 10% heat-inactivated fetal bovine serum plus 0.1% penicillin/streptomycin in a humidified incubator at 37°C (5% CO_2) and passaged about every 4 days. Cells were discarded after ~30 passages. For TIRF experiments, cells were first passaged onto 35-mm plastic tissue-culture dishes and transfected 24 h later with Polyfect reagent (QIAGEN, Valencia, CA) according to the manufacturer's instructions and as previously described (30). The next day, cells were plated onto poly-L-lysine-coated glass-bottomed 35-mm tissue-culture dishes (MatTek, Ashland, MA) and experiments were performed over the following 1–2 days.

Biotinylation assays and immunoblotting

Cells were grown in 100-mm culture dishes and individually transfected with myc-tagged KCNQ1–4 and GFP. After 48 h, the cells were washed three times with phosphate-buffered saline (PBS) at room temperature (22–25°C), and cell-surface proteins were biotinylated by EZ-Link Sulfo-NHS-S-S-Biotin (0.5 mg/mL, Pierce, Rockford, IL) in PBS. After incubation at 4°C for 1 h, the cells were washed five times with ice-cold PBS to remove any remaining biotinylation reagent. Cells were then harvested with a rubber policeman in gentle-lysis buffer (GLB, 75 mM NaCl, 50 mM HCl-Tris, 2 mM EGTA, 1% Nonidot P-40, 10% glycerol) plus the protease inhibitor phenylmethyl-sulfonyl fluoride (PMSF; Sigma, St. Louis, MO), and lysate proteins were quantified with a bicinchoninic acid assay (Pierce). Proteins (150 μg/reaction) were mixed with 50 μL streptavidin-immobilized beads (Pierce; beads were first washed 4× with GLB) overnight at 4°C. The beads were pelleted, washed thoroughly in GLB, and incubated in Laemmli sample buffer at 50°C for 30 min. Bound proteins were separated using sodium dodecyl sulfate polyacrylamide gel electrophoresis (SDS-PAGE), followed by electroblotting onto nitrocellulose membranes. Immunoblots was probed with mouse anti-myc primary antibodies (Clontech) at 1:1000 dilution overnight at 4°C in a blocking solution containing 5% nonfat dry milk (Carnation, Wilkes-Barre, PA) in TBS and Tween-20, and subsequently treated with goat anti-mouse horseradish peroxidase-conjugated secondary antibodies (1:25,000 dilution, 45 min, room temperature; Jackson ImmunoResearch, West Grove, PA). Blots were developed with enhanced chemiluminescence (Supersignal, Pierce) and exposed on X-ray film (Biomax, Rockville, MD).

TIRF microscopy

Fluorescence emissions from enhanced cyan fluorescent protein (CFP)-tagged or enhanced yellow fluorescent protein (YFP)-tagged KCNQ1–5 channels were collected from transiently transfected CHO cells at room temperature using TIRF (also called evanescent field) microscopy. TIRF generates an evanescent field that declines exponentially with increasing distance from the interface between the cover glass and the cytoplasm, illuminating only a thin section (~300 nm) of the cell in contact with the cover glass, including the plasma membrane (31). All TIRF experiments were performed in the TIRF microscopy core facility housed within the Department of Physiology (University of Texas Health Science Center at San Antonio, San Antonio, TX). Fluorescence emissions were collected using an inverted TE2000 microscope with through-the-lens (prismless) TIRF imaging (Nikon, Lewisville, TX). After the medium in the culture dish was replaced with Ringer's solution, samples were viewed through a plane Apo TIRF 60× oil-immersion high-resolution (1.45 numerical aperture) TIRF objective. Coupled to the microscope is a laser light delivery system (Prairie Technologies, Middletown, WI) consisting of a 40 mW argon laser outputting 488 and 514 nm lines and a 442 nm diode pumped solid-state laser. The excitation light was selected with an acoustic optical tunable filter, controlled by Metamorph software. CFP and YFP emissions were simultaneously collected using a Dual-View chip splitter (Optical Insights, Photometrics, Göttingen, Germany) equipped with a filter cube containing HQ470 nm/30 m and HQ550 nm/30 m emission filters for CFP and YFP emissions, respectively, and a 505 nm dichroic mirror for separation of emission wavelengths. The TIRF angle was adjusted by eye to give the signature TIRF illumination to the experimental chamber. Fluorescence images were collected and processed with a 16-bit, cooled, charge-coupled device camera (Cascade 512F; Roper Scientific, Göttingen, Germany) interfaced to a PC

running MetaMorph software. Images were not binned or filtered, with pixel size corresponding to a square of 122 × 122 nm.

Perforated-patch electrophysiology

Pipettes were pulled from borosilicate glass capillaries (1B150F-4, World Precision Instruments, FL) using a Flaming/Brown micropipette puller P-97 (Sutter Instruments, Novato, CA). The pipettes had resistances of 1–2 MΩ when filled with internal solution and measured in standard bath solution. Membrane current was measured with pipette and membrane capacitance cancellation, sampled at 5 ms, and filtered at 200 Hz by means of an EPC-9 amplifier and PULSE software (HEKA/Instrutech, Port Washington, NY). In all experiments, the perforated-patch method of recording was used with amphotericin B (600 ng/mL) in the pipette (32). Amphotericin was prepared as a stock solution as 60 mg/mL in dimethyl sulfoxide. In these experiments, the access resistance was typically 7–10 MΩ 5–10 min after seal formation. Cells were placed in a 500 μL perfusion chamber through which solution flowed at 1–2 mL/min. Inflow to the chamber was achieved by gravity from several reservoirs, selectable by activation of solenoid valves (Warner Scientific, Hamden, CT). Bath solution exchange was complete by <30 s. Experiments were performed at room temperature. The amplitude of the KCNQ current was usually defined as the holding current at 0 mV. In some cells, a more precise measurement was the XE991-sensitive current at the holding potential of 0 mV. CHO cells have negligible endogenous macroscopic K^+ currents under our experimental conditions, and 10 μM XE991 completely blocks the K^+ current in KCNQ-transfected CHO cells, but has no effect on currents in nontransfected cells (30).

Analysis

To estimate voltage dependence, tail current amplitudes were measured at a point 20 ms after the repolarization to −60 mV, normalized, and plotted as a function of test potential. The data were fit with Boltzmann relations of the form $I/I_{max} = I_{max}/\{1 + \exp[(V_{1/2} - V)/k]\}$, where $V_{1/2}$ is the voltage that produces half-maximal activation of the conductance and k is the slope factor. To estimate the affinity for Ba^{2+} block, the data were fit by sigmoidal (logistic) relations of the form: $I/I_o = (max - min)/\{1 + ([Ba^{2+}]/K_D)^p\}$, where K_D is the apparent dissociation constant of Ba^{2+} for the channel producing half block of the current, I_o is the current in the absence of Ba^{2+} ions, and p is the power variable. The *max* and *min* were constrained to be unity and zero, respectively, corresponding to zero or complete block at zero or infinite $[Ba^{2+}]$, respectively. Cell populations were compared using one- or two-tailed *t*-tests when appropriate. The data are given as the mean ± SE.

Homology modeling

Three-dimensional models of the Kv7.3 pore domain (S5-turret domain (TD)-pore helix-selectivity filter (SF)-S6) were constructed using the solved crystal structure of the pore domains of the bacterial channel KvAP (33) as a template (Protein Database accession number 1orqC) and the program SWISS-MODEL (34). Among K^+ channels whose crystal structures have been solved, we chose KvAP as the template on the basis of its highest sequence similarity (34%) to Kv7.3. The initial sequence alignment between Kv7.3 wild-type and KvAP was generated with the full-length multiple alignment of ClustalW. Then the alignment of residues K270–S353 of Kv7.3 to residues K159–N233 of KvAP was submitted for automated comparative protein modeling implemented in SWISS-MODEL (http://swissmodel.expasy.org/SWISS-MODEL.html) using the former sequence as a target protein and the latter as template structure. The carbonα root mean-square (CαRMS) between the Kv7.3 structural model and the template (KvAP) was 0.12 Å for 73 atoms of the aligned amino acids (0.43 Å for 292 backbone atoms). This comparison did not include residues V289–E294 and E299–Y303 from the TD of Kv7.3, which are absent in KvAP. Mutant structural models were selected individually using the program DeepView (Swiss-PdbViewer). Then SWISS-MODEL project files containing the target sequence with a single mutation, and the superposed template structure, were modeled and submitted in the program. To generate the tetrameric Kv7.3 homology models, four identical Kv7.3 subunit models were organized around the signature sequence of the SF (residues 316TIGYGDK322) by superposition onto the segment 196TVGYGDV202 of KvAP. The resulting models were subsequently energy-optimized using GROMOS96 in default settings within the Swiss-PdbViewer. The models with the most likely conformation are represented here.

Solutions and materials

The external Ringer's solution used to record KCNQ currents in CHO cells contained (in mM): 160 NaCl, 5 KCl, 2 $CaCl_2$, 1 $MgCl_2$, and 10 HEPES, pH 7.4 with NaOH. The pipette solution contained (in mM): 160 KCl, 5 $MgCl_2$, 5 HEPES, 10 EGTA, 3 K_2ATP, and 0.1 NaGTP, pH 7.4 with KOH with added amphotericin B (600 ng/mL). Reagents were obtained as follows: DMEM, fetal bovine serum, penicillin, and streptomycin: Invitrogen; ATP, GTP, and NEM, and amphotericin B: Sigma. XE991 and linopirdine were kind gifts from Michael E. Schnee (DuPont Pharmaceuticals, Billerica, MA).

RESULTS

KCNQ channels display divergent macroscopic current amplitudes

We first confirmed the highly differential current amplitudes from the different KCNQ channels that have been widely reported in the literature by us and by others. We used CHO cells as a convenient mammalian expression system that displays very little endogenous ionic currents (30). Cells were transiently transfected with cDNA coding for the appropriate channels, along with EGFP as a reporter for successful transfection. Fig. 1 *A* shows currents from cells expressing KCNQ1–4 homomers or KCNQ2/3 heteromers studied under perforated-patch voltage clamp. Consistent with previous work, cells transfected with KCNQ4 or co-transfected with KCNQ2+KCNQ3 yielded much larger currents than those individually transfected with KCNQ2 or KCNQ3, with KCNQ1 being intermediate. Current densities at 0 mV are summarized in Fig. 1 *B*. For cells transfected with KCNQ1, KCNQ2, KCNQ3, KCNQ4, or KCNQ2+KCNQ3, current densities at 0 mV were 35.7 ± 4.8 ($n = 7$), 10.5 ± 2.3 ($n = 9$), 9.8 ± 2.2 ($n = 17$), 60.9 ± 7.1 ($n = 40$), and 62.5 ± 6.9 pA/pF ($n = 16$), respectively. As a baseline for the chimeric and mutant channels studied below, we quantified the voltage dependence of activation of the wild-type channels by tail-current analysis. As reported in studies from many laboratories, KCNQ1 has the most depolarized voltage dependence, KCNQ3 has the most hyperpolarized, and KCNQ2, KCNQ4, and KCNQ2/3 channels have intermediate voltage dependence (Fig. S1 *A* in Supplementary Material, Data S1). Although the raw differences in macroscopic expression are already large, we wanted to compare their expression taking into account their known single-channel properties, namely, their unitary current amplitude and open probability (P_o) at saturating voltages, so as to estimate the relative number of functional channels underlying these cur-

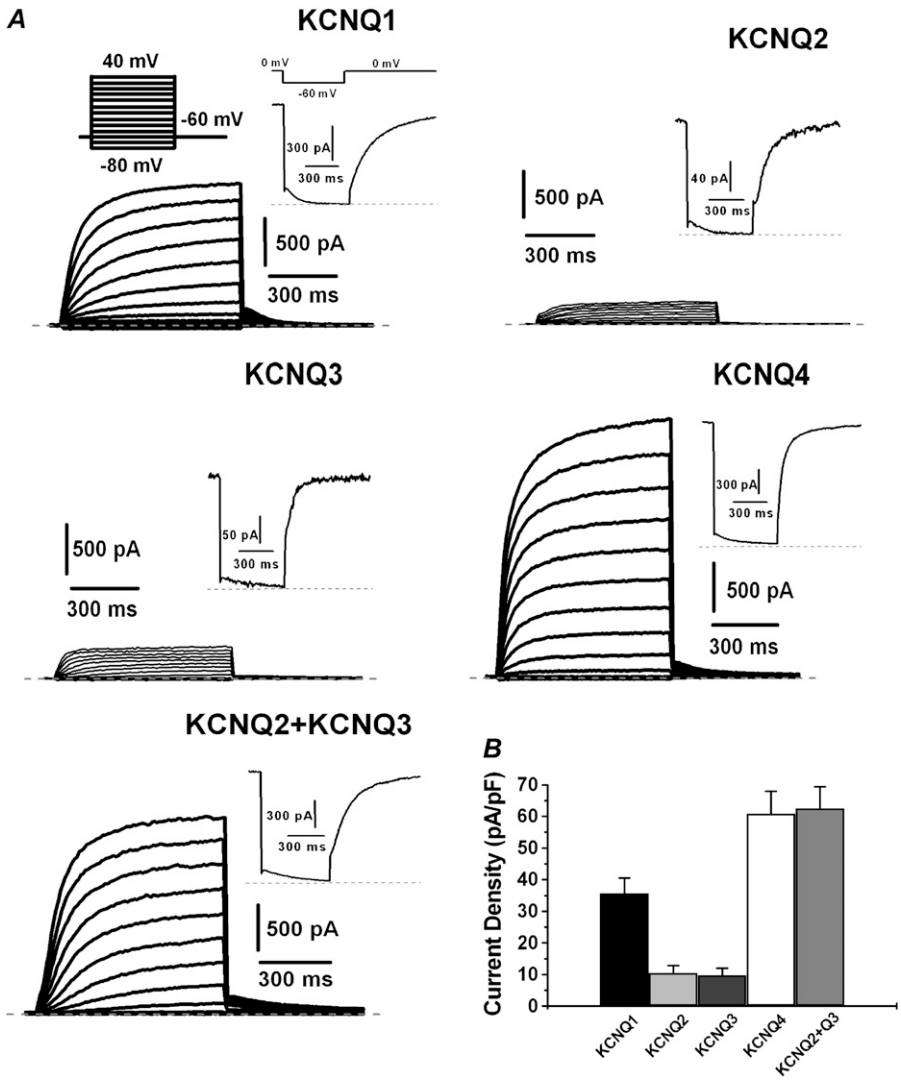

FIGURE 1 KCNQ channels yield widely divergent macroscopic current amplitudes. (*A*) Plotted are families of currents recorded from CHO cells transfected with KCNQ1, KCNQ2, KCNQ3, KCNQ4, or KCNQ2+KCNQ3 studied under perforated-patch voltage clamp. As shown in the inset, cells were held at −60 mV and voltage steps were applied from −80 to 40 mV in 10 mV increments. In the insets are shown representative currents using the ''classic'' M-current protocol (as shown). (*B*) Bars are the summarized current density at 0 mV for the indicated channel type.

rents. For KCNQ1, for which unitary channel openings have not been recorded, we used an upper limit of 0.12 pA measured by fluctuation analysis (24), and the maximal possible P_o of unity, which sets a lower limit for the number of channels necessary to generate the observed KCNQ1 currents. For KCNQ2, KCNQ3, KCNQ4, and KCNQ2/3, we used measured values of 0.55 pA, 0.64 pA, 0.21 pA, and 0.59 pA for their unitary current amplitudes at 0 mV, and published P_o values of 0.17, 0.89, 0.07, and 0.31 (22,25). Based on the macroscopic current density as the product NP_oi, where N is the number of functional channels per unit membrane, P_o is the open probability, and i is the unitary current amplitude, we converted the current densities to N (Table 1) using the above values for P_o and i. For KCNQ1, KCNQ2, KCNQ3, KCNQ4, and KCNQ2/3, N was calculated to be 201, 112, 15.4, 4143, and 342 functional channels/pF, respectively. For KCNQ1, the value of N should be taken as a lower limit. This simple analysis indicates that the densities of functional KCNQ1, KCNQ2, and KCNQ2/3 are roughly parallel, but the density of functional KCNQ3 must be 10–20-fold lower, and that of KCNQ4 must be >10-fold higher. We thus proceeded to investigate the origin of the divergent expression of functional channels.

Differences in plasma-membrane expression of KCNQ2–4 channel protein do not account for differential current amplitudes

Our first measure of surface protein expression was obtained using biotinylation assays and immunoblots to specifically label and quantify the KCNQ channels in the plasma membrane. In these experiments, we focused on KCNQ2, KCNQ3 and KCNQ4, since homomeric and heteromeric channels assembled from these subunits show the greatest divergence in macroscopic current amplitudes. KCNQ2–4 subunits were epitope tagged by introducing the myc epitope to their amino terminus, and individually expressed in CHO cells. After labeling by biotin, cell-surface proteins were isolated by allowing them to bind to streptavidin-conjugated beads. The biotinylated proteins were separated by SDS-PAGE and transferred to nitrocellulose. Lysate from cells

TABLE 1 Differential number of functional channels in the membrane

Channel	Density of functional channels (pF^{-1})
KCNQ1	201*
KCNQ2	112
KCNQ3	15.4
KCNQ4	4143
KCNQ2/3	342
KCNQ3(TD)Q1	30.0
KCNQ1(N289E)	87.2*
KCNQ3(A315T)	397

For each channel, the macroscopic current density (N) was converted to the density of functional channels by using the formula $n = I/P_o i$, where P_o is the open probability, and i is the unitary current, with the values used indicated in the text.

*For these values, the P_o used is the upper limit of unity, and the unitary current was assumed to be the upper limit of 0.12 pA; thus, those values of N should be used as a lower limit.

expressed with wild-type KCNQ3 was not labeled, showing the specificity of the myc antibodies, and lysate from nonbiotinylated cells was not retained by the streptavidin beads, showing specific binding to the beads (data not shown).

We investigated the surface protein expression from cells transfected individually with myc-tagged KCNQ2–4 channels, cotransfected with myc-tagged KCNQ2 + wild-type KCNQ3, with myc-tagged KCNQ3 + wild-type KCNQ4 or with wild-type KCNQ3 + myc-tagged KCNQ4. The latter two conditions were tested due to the report of the heteromeric assembly of KCNQ3 and KCNQ4, in which cotransfection of wild-type KCNQ3 with KCNQ4 strongly increased the current amplitude and cotransfection of a nonfunctional pore-mutant KCNQ3 reduced it (14). Shown in Fig. 2 *A* are immunoblots of the cell-surface (*top row*) and total lysate (*bottom row*) protein. The amount of protein in the lanes of the blot was estimated by measuring the pixel intensity of their corresponding antibody-labeled bars. To control for differing channel proteins made by the cells, the data were quantified as the ratio of surface/total protein for each individual experiment. For the homomeric channels, we first wished to compare the surface protein expression to KCNQ4, which yields far larger homomeric currents than KCNQ2 or KCNQ3 (18,21) (this study). Since the currents from heteromeric KCNQ2/3 channels are much larger than those from KCNQ2 or KCNQ3, we also wished to compare them to the surface protein from KCNQ2+KCNQ3 cotransfections. Similarly, we also compared the surface protein expression of KCNQ3+KCNQ4 to that of KCNQ4 alone. Thus, the normalized surface protein of KCNQ2 or KCNQ3 is plotted as the ratio to KCNQ4, as well as to KCNQ2+KCNQ3, and that from KCNQ3+KCNQ4 to that of KCNQ4 (Fig. 2 *B*). These data indicate no difference in surface protein for KCNQ2 or KCNQ3 homomers compared with KCNQ2/3 heteromers, suggesting that the six- to sevenfold greater density of KCNQ2/3 currents versus KCNQ2 or KCNQ3 is not due to differences in membrane expression of channel protein. Likewise, the data suggest that the greater current amplitude from KCNQ3/4 channels, relative to KCNQ4 alone, is not due to greater surface protein expression of KCNQ4 subunits. Among KCNQ2–4 homomers, the data indicate about a threefold greater membrane protein expression of KCNQ4 versus KCNQ2 or KCNQ3. However, these differences are relatively modest, and as Table 1 indicates, they fall some 12-fold or 90-fold, respectively, less than what would be necessary, to account for the dramatic differences in functional KCNQ2 or KCNQ3 channels that must be present to account for their respective macroscopic currents.

Our second assay for plasma-membrane expression was performed by examining individual living cells using TIRF microscopy (31,35). TIRF illumination involves directing a laser beam at the interface between two transparent media of differing refractive indices at a glancing angle. By the laws of optics, at an angle greater than the critical angle determined by ratio of the two refractive indices, the light beam is not primarily transmitted to the second media, but is instead reflected; however, a component does penetrate into the second media as an ''evanescent wave'' that decays exponentially in intensity over a distance of only several hundred nanometers. Thus, we can selectively excite only fluorophores located within ~300 nM of the plasma membrane by directing laser light at such a glancing angle through a special TIRF objective (36). Any molecules located deeper in the cytoplasm will not be illuminated, as evidenced in our facility by control experiments involving cytoplasmic, endoplasmic reticulum-targeted, or membrane-targeted fluorescent proteins (22,37,38). We constructed CFP-tagged KCNQ1–5 and expressed them in CHO cells. Membrane abundance of the channels was estimated by measuring the pixel intensity of images taken under TIRF illumination, using 442-nm excitation light from a blue-diode laser. Fig. 2 *B* (*upper*) shows representative images of robustly expressing channels in the membrane, as previously observed (22,38). All images were taken using the same laser intensity and camera exposure settings, and the cell-free background intensity has been subtracted from all measurements. The pixel intensities of such images are summarized in Fig. 2 *B* (*lower*), which was not significantly different between KCNQ1–5 homomers or between KCNQ2/3 heteromers and any of the homomeric channels. Thus, the TIRF microscopy data also indicate little differences in surface expression of the channels, and that differential membrane abundance of channel protein does not underlie the differences in macroscopic current amplitudes.

The TD is a determinant of macroscopic current amplitudes

Given the large difference in functional channels between KCNQ3 and either KCNQ1 or KCNQ4, we pursued a chimeric or mutagenesis approach to identify the molecular determinants for current amplitudes. The region between the fifth and sixth transmembrane domains (S5 and S6) of K^+ channels contains the pore structure, comprised sequentially

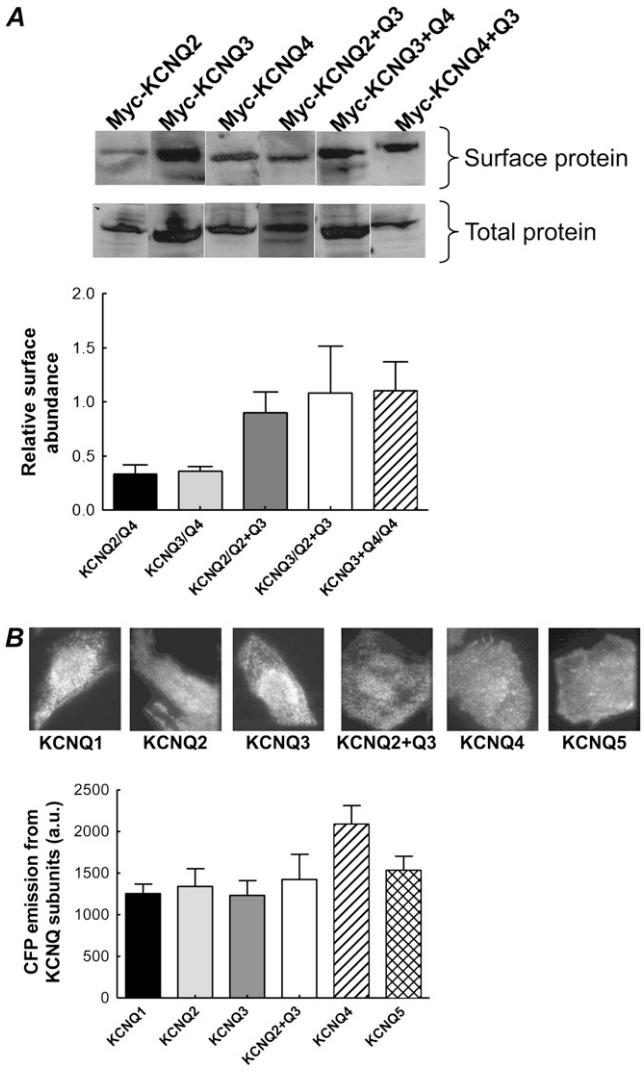

FIGURE 2 Differential surface protein expression does not explain the divergent current amplitudes of KCNQ channels. (*A*) Shown are representative biotinylation experiments for the indicated channels. The indicated subunit was myc-tagged. The upper panels show the biotinylated (surface) myc-tagged protein, and the lower panels show the total myc-tagged protein from whole-cell lysates. (*B*) Bars show summarized biotinylation data. For each experiment, the ratio of surface/total protein was calculated to estimate relative surface expression. These values were then compared with those of the indicated channel. Those values of KCNQ2/Q4, KCNQ3/Q4, KCNQ2/Q2+Q3, KCNQ3/Q2+Q3, and KCNQ3+Q4/Q4 (data pooled from both types shown in the last two lanes in *A*) were 0.33 ± 0.09 ($n = 6$), 0.36 ± 0.04 ($n = 12$), 0.90 ± 0.19 ($n = 6$), 1.08 ± 0.43 ($n = 6$), and 1.1 ± 0.27 ($n = 8$). (*B*) Representative TIRF imaging experiments used to quantify membrane expression of KCNQ channels. Upper panels show fluorescent images under TIRF illumination of CHO cells expressing CFP-tagged KCNQ1–5 or KCNQ2+3 channels. In all cases, CHO cells were transfected with a total of 5 μg cDNA; for KCNQ2+3, 2.5 μg cDNA was used for each. The emission was quantified by measuring the mean pixel intensity of the outline of the cell for each image, with the background intensity in a cell-free area subtracted. The camera exposure time, laser intensity, and TIRF aperture setting remained the same for each cell and channel type. Bars show summarized data for each channels type, plotted as mean pixel intensity on the ordinate ($n =$ 21–22 cells).

of the (extracellular) TD, a short pore helix, and the SF (39). Fig. 3 shows a sequence alignment of the pore structure of KCNQ1–4 channels, as well as the *Shaker* channel, whose pore structure has been subjected to intensive mutagenesis, and the prokaryotic KcsA and KvAP channels, whose atomic structures have been solved (33,39). The alignment includes an algorithm that takes into account the continuity of predicted secondary structure. Indicated on this alignment are the chimeras and mutations within this region examined in this study. Upon inspection, a glaring feature of KCNQ3, unique among the others, is its extended TD. In K^+ channels, the TD contains several sites involved in scorpion toxin binding (40,41) and forms part of the external vestibule of the pore. In oocytes, the TD has been shown as one locus conferring large versus small macroscopic currents in KCNQ channels (20). We tested the effect of the TD in mammalian cells by expressing a chimera consisting of KCNQ3 with the TD of KCNQ1 and examining the resultant currents under perforated-patch voltage clamp. This KCNQ3(TD)Q1 construct (kindly given to us by Michael Schwake, Christian Albrechts University, Germany) has residues 287–302 in KCNQ3 replaced with residues 288–301 of KCNQ1 (Fig. 3). Indeed, replacement of the KCNQ3 TD with that of KCNQ1 increased macroscopic current density, to 32.8 ± 4.6 pA/pF ($n = 8$, $p < 0.001$; Fig. 4, *A1* and *B*). To determine whether the TD affects the single-channel properties of the channels, we performed cell-attached recording experiments. Representative sweeps at 0 mV are shown in Fig. 4 *A* (*inset*). The single-channel current and P_o of the KCNQ3(TD)Q1 chimera was 1.35 ± 0.17 pA and 0.81 ± 0.09 ($n = 4$), both somewhat higher than that suggested previously using noise analysis (20). The twofold increase in the unitary current suggests that the TD architecture influences the permeation pathway of KCNQ channels, consistent with it being a part of the pore structure (39). However, the TD replacement did not affect the saturating P_o, which for KCNQ channels is thought to be determined by binding of PIP_2 to the carboxy-terminus (25). Of interest, the TD replacement affected the voltage dependence of activation, which was now intermediate between that of KCNQ3 and KCNQ1 (Fig. S1 *B* in Data S1). Using the same analysis as in Fig. 1, we estimated the density of functional KCNQ3(TD)Q1 channels to be 30.0 channels/pF, an increase of about twofold over wild-type KCNQ3 (Table 1). Thus, the increased current density produced by replacement of the KCNQ3 TD with that of KCNQ1 (this study and Schenzer et al. (20)) appears to be about half due to an increase in the density of functional channels in the membrane, and about half due to an increase in the unitary current of the chimeric channel. We further tested whether the TD swap resulted in greater numbers of channels in the membrane by using TIRF image measurements as before on YFP-tagged channels. However, compared to YFP-tagged KCNQ1 and KCNQ3, fluorescence from YFP-tagged KCNQ3(TD)Q1 channels was not significantly different (Fig. S3 in Data S1).

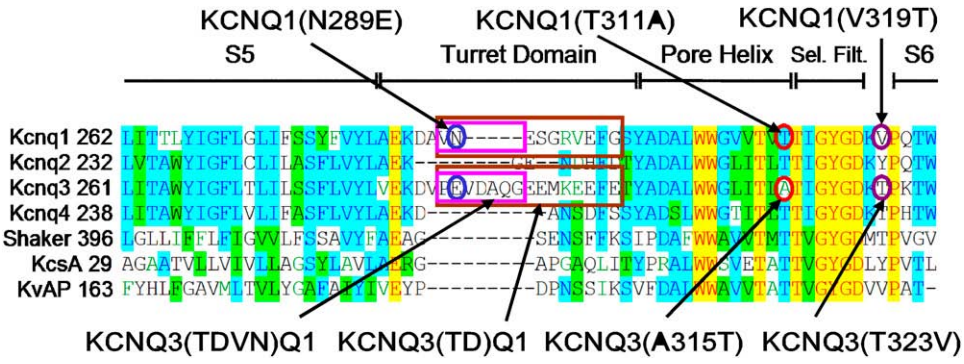

FIGURE 3 Sequence alignment of the pore region investigated in this study. Shown from the distal part of the fifth membrane-spanning domain (S_5) to the proximal part of S_6 is an alignment of KCNQ1–4, the *Shaker* K^+ channel of *Drosophila*, and the bacterial K^+ channels KcsA and KvAP. The domains or residues exchanged or mutated in KCNQ1 or KCNQ3 are indicated. Only mutants that gave functional currents are shown. The alignment was performed using the program Vector NTI, which takes into account secondary structure in the alignment algorithm. Yellow, blue, and green indicate consensus residues that are completely conserved, consensus residues derived from a block of similar residues at that position, and consensus residues derived from the occurrence of a given residue in greater than half of the aligned molecules, respectively.

We then proceeded to more carefully dissect out the determinants within the TD necessary for this doubling of channel expression. Previous work has suggested that the TD action is mediated by glycosylation of an asparagine at residue 289 of KCNQ1 that KCNQ3 does not possess (20). To test the importance of this asparagine, we mutated it to the glutamate that KCNQ3 has at this position. Such KCNQ1(N289E) mutant channels displayed a voltage dependence of activation unchanged from wild-type KCNQ1 (Fig. S1 *B* in Data S1) but yielded current densities that were reduced by about half compared to wild-type KCNQ1 (Fig. 4, *B* and *E*). Within the TD, the proximal half is most divergent between KCNQ1 and KCNQ3. Indeed, whereas KCNQ3 contains PEVDAQG, KCNQ1 has only VN and a five-residue gap in the alignment with KCNQ3 (Fig. 3). We tested a more focused chimera in which the PEVDAQG was replaced by VN (KCNQ3(TDVN)Q1), and found this swap to result in current amplitudes not significantly different from the full KCNQ3(TD)Q1 chimera (Fig. 4, *C* and *E*), but with a slightly less depolarized voltage dependence of activation (Fig. S1 *B* in Data S1). We also tested a swap within the latter half of the TD, in which EMKE in KCNQ3 was replaced by SGRV of KCNQ1, but that construct did not express ($n = 12$). Likewise, a swap of the final two residues of the KCNQ3 TD, ET, by the GS of KCNQ1 did not result in measurable currents ($n = 12$). Thus, we conclude that the twofold increases in the density of functional channels conferred by replacement of the KCNQ3 TD by that of KCNQ1 localizes to an asparagine possessed by the TD of KCNQ1. Although we did not test N-glycosylation directly, this result is consistent with previous work (20).

The carboxy terminus of KCNQ channels contains four conserved helices, named A–D (42). Several studies have indicated that the distal two helices (C–D), thought to be coiled-coiled in nature, are involved in the assembly of functional channels (19,26,27). Thus, we wished to know whether the effects of the TD and the C–D helices are additive. We constructed a triple chimera in which most of the carboxy terminus of the KCNQ3(TD)Q1 chimera was replaced with that of KCNQ4. The carboxy-terminal junction point was just after the first conserved domain, called the A helix (42), and so both coiled-coiled domains are those of KCNQ4. The resulting KCNQ3(TD)Q1-(CT)Q4 triple chimera yielded a current density ~4-fold larger than that of the KCNQ3(TD)Q1 chimera (Fig. 4, *D* and *E*), indicating that the effect of the carboxy terminus is mostly additive with that of the TD. The voltage dependence of activation of the triple chimera was slightly less depolarized compared to wild-type KCNQ3 (Fig. S1 *B* in Data S1). The data in this section are summarized in Fig. 4 *E*. For KCNQ(N289E), KCNQ3(TDVN)Q1, and KCNQ3(TD)Q1-(CT)Q4, the current densities at 0 mV were 15.5 ± 2.9 pA/pF ($n = 8$, $p < 0.01$), 53.2 ± 14.4 pA/pF ($n = 9$, $p < 0.001$), and 125 ± 18 pA/pF ($n = 8$, $p < 0.001$), respectively.

Mutation at the internal, not the external, TEA^+ binding site has dramatic effects on current amplitudes

In *Shaker*-type K^+ channels, large effects on macroscopic currents are caused by ''C-type'' inactivation, which is widely thought to be mediated by structural rearrangements of the SF or pore-helix residues (43). Given the effect of the TD sequence on KCNQ3 currents, we wondered whether the lack of correlation between surface expression and current amplitudes of KCNQ3 were reflective of the residence of many channels in a long-lived dormant state analogous to C-type inactivation. A dominant locus determining the extent of C-type inactivation of *Shaker* channels is the binding site for external tetraethylammonium (TEA) ions; for example, mutation of the native threonine to a glutamate or a lysine at the 449 position in *Shaker* speeds C-type inactivation by 100-fold, whereas a valine at 449 abolishes it (44). KCNQ1 has a valine in that position, whereas KCNQ3 has a threonine (Fig. 3). We tested whether a similar mechanism might be involved in KCNQ channels by swapping these residues between KCNQ1 and KCNQ3. However, we found that KCNQ3(T323V) channels yielded currents even smaller than wild-type KCNQ3 (2.2 ± 1.4 pA/pF, $n = 6$) (Fig. 5, *A* and *C*). The inverse mutant, KCNQ1(V319T), yielded currents that

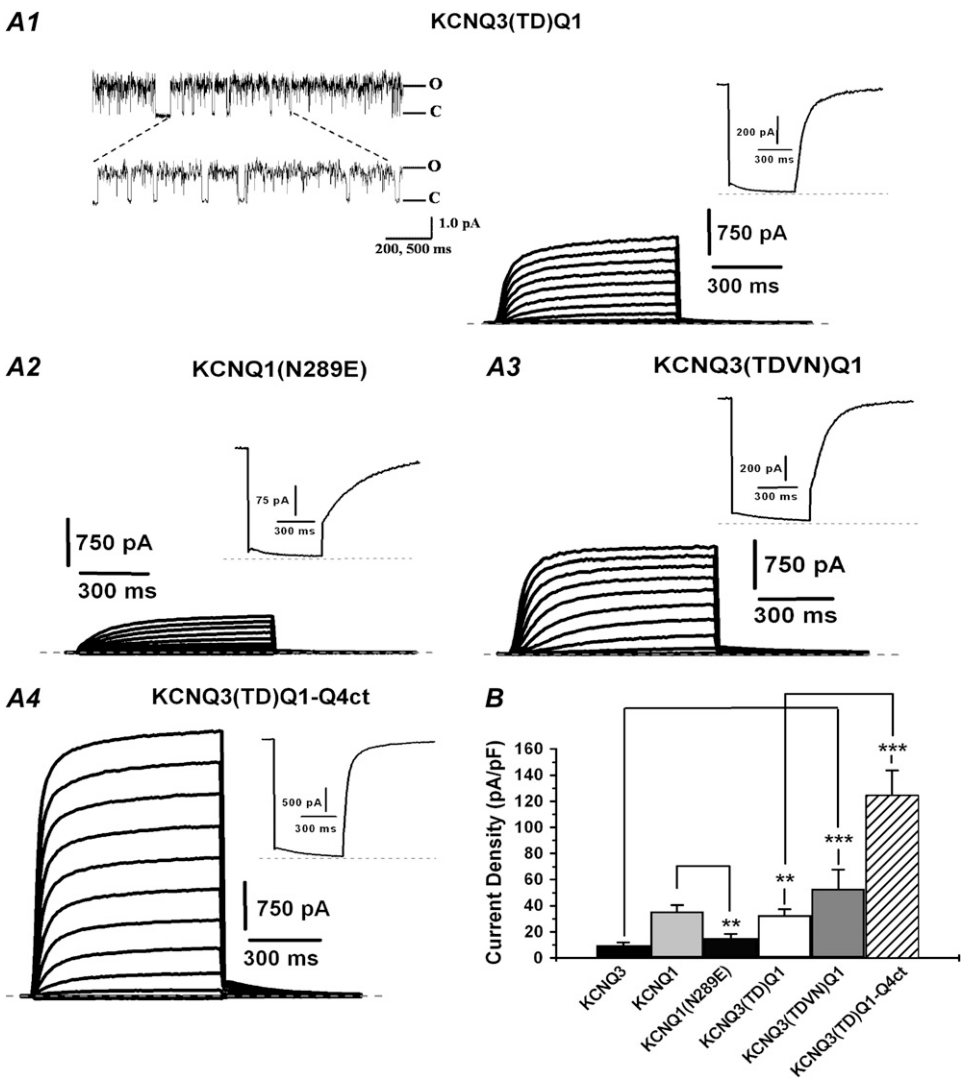

FIGURE 4 The TD of KCNQ1 increases current amplitudes of KCNQ3. Shown are representative current families from CHO cells, studied under perforated-patch clamp, expressing the KCNQ3(TD)Q1 chimera (*A1*), the KCNQ1 (N289E) point mutant (*A2*), the KCNQ3(PEVDAQG-VN) replacement (*A3*), or the KCNQ3(TD)Q1-Q4ct triple chimera (*A4*). The pulse protocol used was the same as in Fig. 1. In the insets are shown representative current traces using the ''classic'' M-current protocol. Also shown for KCNQ3(TD)Q1 is a representative current trace from a cell-attached patch containing a single channel at the patch potential of 0 mV. An expanded view of the single-channel current record is shown below. Note the high P_o of this chimera, similar to wild-type KCNQ3. (*B*) Bars show summarized current densities for the indicated channel studied under perforated-patch clamp. $^{**}p < 0.01$, $^{***}p < 0.001$.

were somewhat smaller than those from wild-type KCNQ1 (21.1 ± 1.3 pA/pF, $n = 8$, $p < 0.01$), but still substantial, with no enhancement of macroscopic inactivation that was apparent (Fig. 5, *A* and *C*). Another signature characteristic of C-type inactivation is its dependence on extracellular $[K^+]$ or species of permeant ion, such that high $[K^+]_o$ reduces the rate and extent of the inactivation (44). We thus compared KCNQ3 currents under normal Ringer's (5 mM K^+) or a high-K^+ Ringer's (150 mM K^+) in the bath. However, we found that raised $[K^+]_o$ did not increase the amplitude of the current, but rather reduced it, as expected from the Nernst equation (Fig. 5 *B*). In normal or high-K^+ Ringer's, the KCNQ3 current density at 40 mV was 19.2 ± 2.5 and 10.3 ± 1.9 pA/pF, respectively (Fig. 5 *C*, $n = 7$ and 6). Thus, both tests suggest that the smaller current density of KCNQ3 channels is not due to a classical C-type inactivation mechanism.

We then investigated the effect of mutation of the internal TEA binding site, which in *Shaker* is T441, corresponding to T311 and A315 in KCNQ1 and KCNQ3, respectively. The pore structure alignment (Fig. 3) shows KCNQ3 to be unique in having an alanine at this position. Etxeberria et al. (15) previously showed this residue to be important for current amplitudes in oocytes, and we obtained the same result in CHO cells. Indeed, the A315T mutation in KCNQ3 dramatically increased the current density by nearly 15-fold relative to wild-type KCNQ3, to 135 ± 28 pA/pF ($n = 12$), and the inverse mutation T311A in KCNQ1 reduced the current density by 10-fold relative to wild-type KCNQ1, to 2.5 ± 1.3 pA/pF ($n = 7$) (Fig. 6, *A*, *B*, and *E*). To determine whether the dramatic effect of the A315T mutation in KCNQ3 is also partly due to alterations in unitary channel properties, we analyzed this mutant in cell-attached patches as well. Fig. 6 *A* (*inset*) shows representative current sweeps at 0 mV. The single-channel current and P_o were 0.40 ± 0.02 pA and 0.85 ± 0.12 ($n = 3$), respectively. This unitary current amplitude is slightly smaller than wild-type KCNQ3, and the P_o is unchanged. Using the same NP_oi analysis as before, we estimate the density of functional KCNQ3(A315T) channels in the membrane to be 397 channels/pF, an increase of 26-fold over wild-type KCNQ3

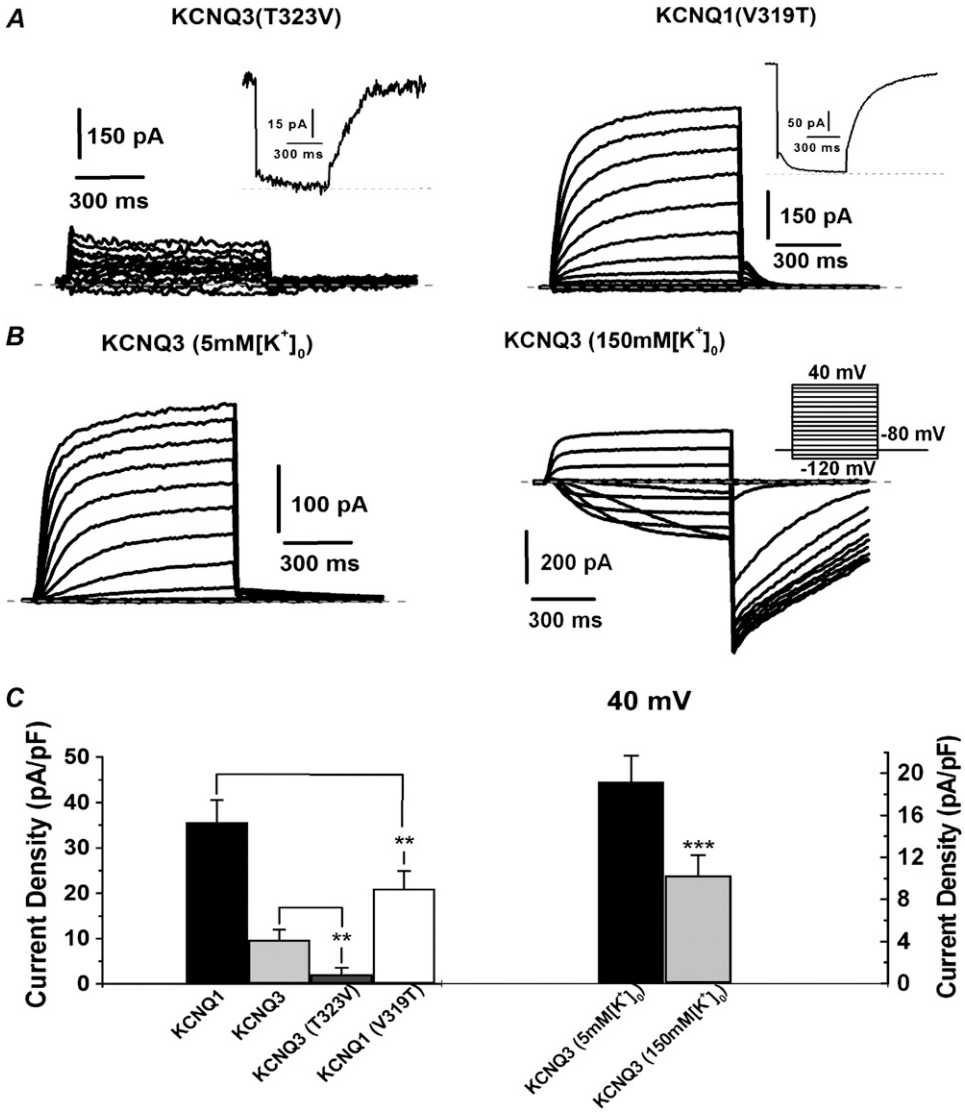

FIGURE 5 C-type inactivation does not underlie the small current expression of KCNQ3. (*A*) Representative current families from CHO cells, studied under perforated-patch clamp, expressing KCNQ3(T323V) or KCNQ1(V319T). (*B*) Representative current families from CHO cells expressing wild-type KCNQ3 channels, studied under perforated-patch clamp with either normal (5 mM K^+), or elevated (150 mM K^+) in the bathing solution. The voltage protocol used in the former is as in Fig. 1; in the latter, cells were held at −80 mV, and a family of voltage steps were applied from −120 to 40 mV, in 10 mV increments (*inset*). (*C*) Bars are summarized current densities at 0 mV for the indicated channels studied in *A* (*left*), or at 40 mV for KCNQ3 studied under 5 mM or 150 mM K^+ (*right*).

(Table 1). The A315T mutation involves substitution of a small hydrophobic residue with a bulkier hydrophilic one. To determine whether side-chain size or hydrophobicity is more important, we also tested the effect of mutating A315 to either a valine or a serine. The former substitution maintains hydrophobicity but increases side-chain size, whereas the latter maintains small side-chain size but is hydrophilic. We found that the A315S mutation resulted in dramatically increased current density (169 ± 15 pA/pF, $n = 9$), similar to the profound increase seen in the A315T mutation (Fig. 6, *C* and *E*). However, the A315V mutation resulted in a very small current density (6.5 ± 0.4 pA/pF, $n = 7$), similar to wild-type KCNQ3 (Fig. 6, *D* and *E*). These data suggest that a hydrophilic residue at this position is important in conferring large currents. Of interest, KCNQ3 is the only member of this family that has a hydrophobic residue in this position; all the others possess a threonine and all yield large homomeric currents if there is sufficient PIP_2 abundance in the membrane. None of the mutants at this position changed the voltage dependence of activation compared to their wild-type background channel (Fig. S1 *B* in Data S2). We also tested whether KCNQ3(A315T) mutant subunits expressed with wild-type KCNQ2 would yield larger currents than those from wild-type KCNQ2+3 channels. Indeed, the current densities from the former were about double those of the latter (Fig. S2 in Data S1and Fig. 6 *E*), suggesting that the effect of the A315T mutation in KCNQ3 enhances currents when it is incorporated into a heteromer, as well as when it is homomeric. Finally, to determine whether the dramatic increase in the density of functional KCNQ3(A315T) channels was due to an increase in the abundance of channel protein in the membrane, we again performed a TIRF microscopy analysis. KCNQ3(A315T) was YFP-tagged, and images were acquired as above under TIRF illumination. However, there was no significant difference between the YFP emission from wild-type KCNQ3 and KCNQ3(A315T) channels (Fig. S3 in Data S1). We also compared the expression of wild-type KCNQ1 to KCNQ1 (T311A) by tagging those channels

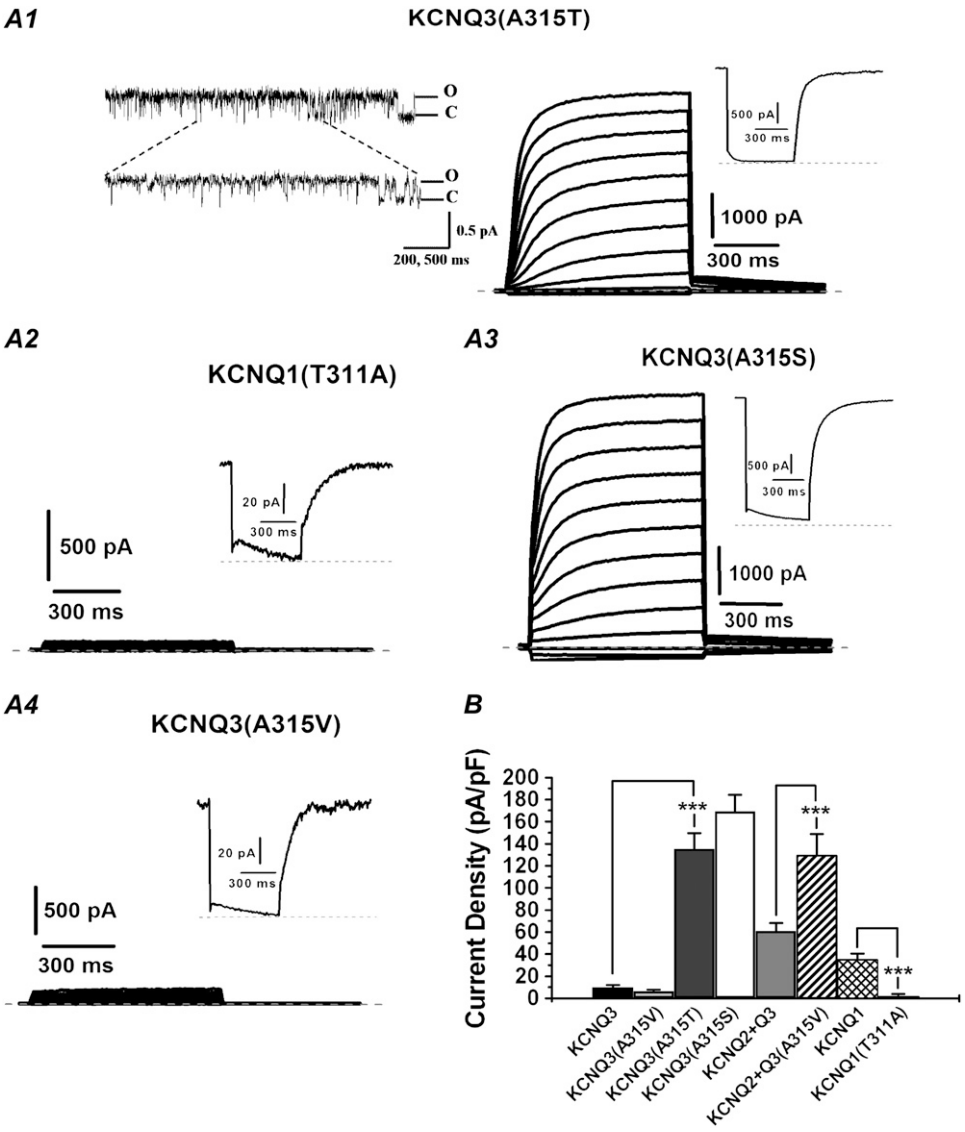

FIGURE 6 A hydrophilic residue at the intracellular TEA^+ binding site confers large current expression. (*A*) Representative current families from CHO cells, studied under perforated-patch clamp, expressing KCNQ3(A315T) (*A1*), KCNQ1 (T311A) (*A2*), KCNQ3(A315S) (*A3*), or KCNQ3(A315V) (*A4*). The pulse protocol used was the same as in Fig. 1. In the insets are shown representative current traces using the ''classic'' M-current protocol. Also shown for KCNQ3(A315T) is a representative current trace from a cell-attached patch containing a single channel at the patch potential of 0 mV. An expanded view of the single-channel current record is shown below. Note the high P_o of this mutant, similar to wild-type KCNQ3. (*B*) Bars show summarized current densities for the indicated channel studied under perforated-patch clamp. $^{**}p < 0.001$.

with YFP and evaluating their emission under TIRF illumination. Although the T311A mutation reduced the KCNQ1 whole-cell current density by 10-fold, there was again no significant difference in membrane expression as measured by TIRF microscopy (Fig. S3 in Data S1). We conclude that the dramatic differences in current density caused by these pore-loop mutations were not due to differential expression of channel proteins in the membrane.

The A315T mutation dramatically increases the sensitivity of KCNQ3 channels to block by external Ba^{2+}

Our data suggest that the divergent density of functional KCNQ channels does not arise primarily from differential surface expression, but rather as a result of other factors. A plausible hypothesis is that there are unique structural features of KCNQ3 that render most of those channels nonfunctional, resulting in a noncorrelation between surface expression and current density. Because its ionic radius is so similar to that of K^+, Ba^{2+} ions can easily enter the pore of K^+ channels (45), where they block diverse K^+ currents, including those of KCNQ channels (46–48). Elegant work on Ca^{2+}-activated K^+ (BK) channels has used Ba^{2+} ions as a probe of the pore, revealing competition between Ba^{2+} and K^+ for the same binding sites in the single-file region of the pore, with the site of Ba^{2+} block situated between external and internal ''lock-in'' sites where K^+ pauses during permeation (49,50). Consistent with this conclusion, the crystal structures of KcsA soaked in the presence or absence of Ba^{2+} ions show the site of block to be at the innermost permeant ion site in the SF (51), very near to where A315 is located in KCNQ3. Thus, we used Ba^{2+} block as a probe for structural alterations in the inner part of the SF induced by the A315T mutation, by comparing the sensitivity of wild-type and A315T channels to block by external Ba^{2+} ions. Indeed, the

A315T mutation increased the apparent K_D for Ba^{2+} block by eight- to 28-fold. Currents were recorded over a range of potentials and Ba^{2+} concentrations from wild-type (Fig. 7 *A*) and A315T KCNQ3 channels (Fig. 7 *B*) and the data at −10 and 30 mV fit by sigmoidal relations (Fig. 7 *C*). For wild-type (but not A315T) channels, the Ba^{2+} block was clearly voltage dependent, leading to an increased difference in sensitivity between wild-type and mutant channels at 30 mV vs. −10 mV. At −10 mV the apparent K_D values were 1.1 ± 0.08 mM and 0.13 ± 0.06 mM, and at 30 mV they were 4.3 ± 0.7 mM and 0.15 ± 0.10 mM for wild-type ($n = 10$) and A315T ($n = 12$) channels, respectively. The altered sensitivity to Ba^{2+} block is not due to differences in P_o, since those values for wild-type and A315T channels are the same. Since the site of Ba^{2+} block of K^+ channels has been localized to the inner part of the SF (49,50), these results suggest that A315T channels have an altered structure in that region of the pore. Below, we form a hypothesis for the mechanism by which this might occur.

Structural homology modeling of the pore region suggests that the A315T mutation makes the SF of KCNQ3 more stable

To gain insight into such a possible structural mechanism, we performed homology modeling of the region around the pore of wild-type and mutant KCNQ3 channels with very divergent current amplitudes, using as the template a K^+ channel for which the solved crystal structure is available. We were especially motivated by recent work from the MacKinnon and Perozo laboratories suggesting that the SF of bacterial KcsA K^+ channels exists in alternate ''conducting'' and ''nonconducting'' conformations induced by the presence or absence of K^+ ions, or determined by the presence of glutamate versus alanine at position 71, respectively (52–55). Among the solved KcsA, KvAP, and Kv1.2 structures, the KvAP channel has the most conserved sequence similarity with KCNQ3 in the region between S5 and S6, inclusive; thus we used this channel as the template for our modeling.

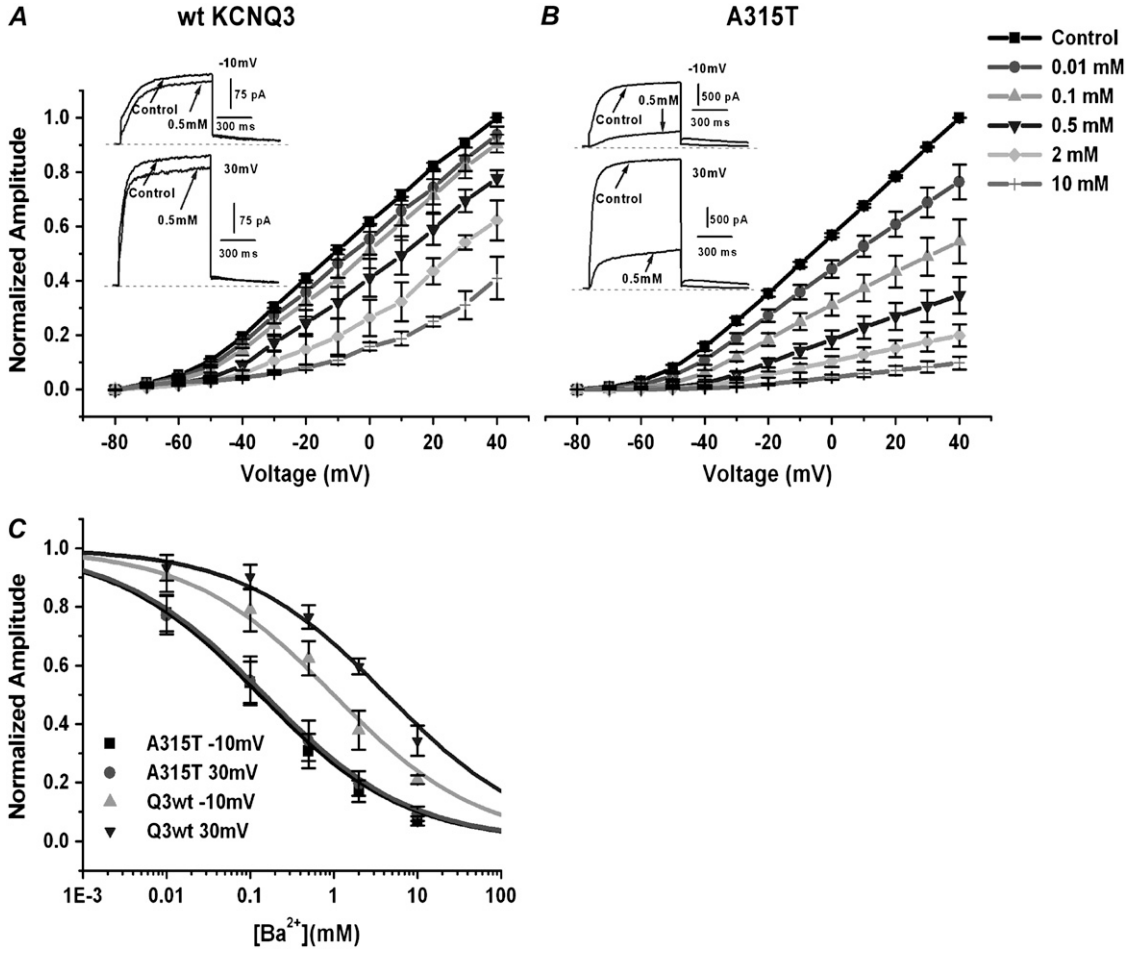

FIGURE 7 The A315T mutation increases the sensitivity of KCNQ3 channels to block by external Ba^{2+} ions. CHO cells were transfected with either wild-type or A315T KCNQ3 channels and studied under perforated-patch voltage clamp. Plotted are the normalized current amplitudes from wild-type (*A*) or A315T (*B*) KCNQ3 channels over a range of voltages and external Ba^{2+} concentrations, with representative current traces at −10 mV or 30 mV shown in the insets. (*C*) The data at −10 mV and 30 mV were summarized as a dose-response plot of normalized current versus [Ba^{2+}], and the data fit by sigmoidal (logistic) relations, with the K_D values given in the text. All four fits had very similar power exponent values, in the range of 0.47–0.52.

The region around the pore of KCNQ3 was modeled using the program SWISS-PROT and the structure of KvAP (33) as the template (see Materials and Methods for details). The CαRMS deviation of the backbone in this region between KCNQ3 and KvAP was 0.59 Å. A primary mechanism of K^+ selectivity has been ascribed to SF carbonyls that make intimate contact with permeating ions, with the side chains pointing away from the permeation path. In particular, the tyrosine in the signature GYG motif, together with pore-helix tryptophans with which it makes hydrogen bonds, is thought to form a ''cuff'' that holds the SF carbonyls at just the right distance to select K^+ over Na^+ (39). In our modeling, we posed two questions: 1), how do the A315 mutations affect the distance between diagonally-opposing residues in the SF; and 2), how might the predicted stability of the SF differ between the structures? We first examined a ''slice'' through the SF at the position of the second ion-binding site (S_2), partly coordinated by Y319 (56), which is hypothesized to collapse in the absence of permeant ions (52,53). However, a comparison between wild-type and A315T KCNQ3 in the positions of Y319 and the double W308,309 residues with which it makes hydrogen bonds showed only slight differences (data not shown). Examining the SF as a whole, Fig. 8 *A* shows the predicted superimposed structures of the SF and distal pore helix of two diagonally opposite subunits of the wild-type and A315T KCNQ3 channels. Also indicated are the predicted distances between the SF GYGI carbonyls of diagonally facing subunits for the wild-type (Fig. 8 *B*) and A315T (Fig. 8 *C*) channels. The five known sites of permeant ion occupancy in the SF (57) are indicated. Although the predicted structures are similar, there are some important deviations, especially the distance between G320 of opposing subunits that are critical for the first-ion binding site (S_1), for which the distance between opposing G320 carbonyls increases from 6.84 Å in the wild-type to 7.37 Å in A315T. Of interest, constriction of the SF at the level of the S_1 binding site has been postulated as a mechanism of C-type inactivation (55,58,59). Within the GYGIT residues that comprise the SF of KCNQ3, the CαRMS deviation between the wild-type and A315T channels was 0.13 Å.

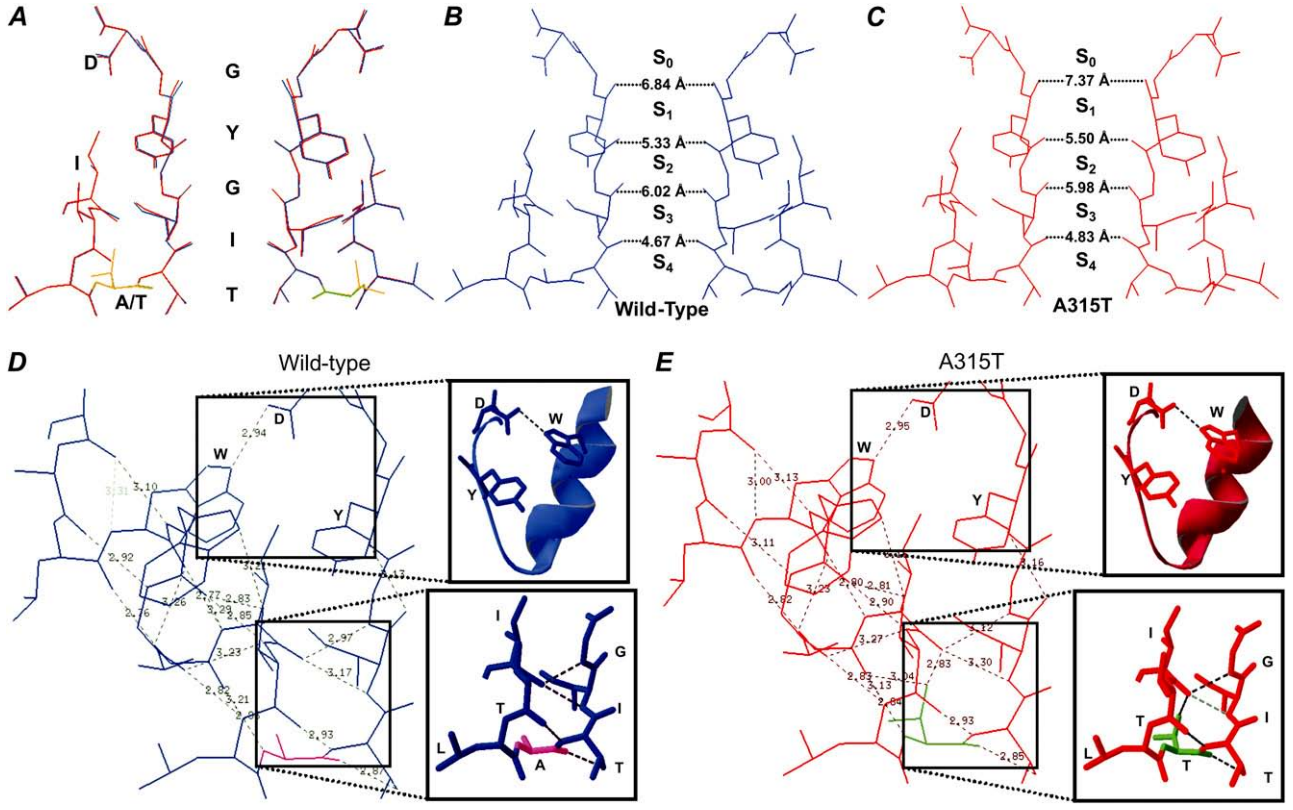

FIGURE 8 Comparison of the structure of the SF region of wild-type and A315T KCNQ3 predicted by homology modeling and the predicted critical H^+-bonding networks within the pore region. After performing a sequence alignment between all of Kv7.3 and KvAP, residues 270–353 of Kv7.3 were modeled using the corresponding residues 159–233 of KvAP as template (see Materials and Methods for details). (*A*) Shown are the superimposed predicted structures of this region from two diagonally-facing subunits of wild-type (*blue*) and A315T KCNQ3 (*red*). The GYGIT of the SF are indicated, along with the D321, I312, and A315 residues focused on in the next figures. Shown are the predicted structures of residues 270–353 of wild-type (*B*) and A315T (*C*) KCNQ3. The distances between the carbonyls of GYGI residues from diagonally facing subunits are indicated, and the positions of the S_0–S_4 permeant ion sites are labeled. Shown are the predicted structures and H^+-bonds within and between the pore helix and SF of wild-type (*D*) and A315T (*E*) KCNQ3. The predicted distances (Å) between donor and acceptor for each bond are indicated. In the insets are shown expanded views (rotated by 180°) of the predicted interaction between D321 and W308, and the mini-network of predicted interactions between the GIT of the SF and the pore helix, in the area around A315 (*D*) or T315 (*E*).

The full networks of predicted hydrogen-bonding interactions within and between the pore helix and the SF of wild-type and A315T channels are shown in Fig. 8, *D* and *E*, respectively. For both wild-type and A315T channels, there are many predicted hydrogen bonds within the pore helix, and between the pore helix and the SF. We particularly focused on two potentially critical hotspots. The first contains interactions between the lower pore helix and lower SF that might differ in the A315 mutants. The second is at the top of the SF, where a critical interaction between D80 and W67 in KcsA (D321 and W308 in KCNQ3) is thought to be destabilized by the E71A mutation, converting channels to a structural variant in which C-type-like inactivation cannot occur (54). However, the A315T mutation in KCNQ3 is not predicted to alter the interaction between D321 and W308; strong H^+-bonding between the oxygen atom of D321 and the nitrogen in the aromatic ring of W308 residues are predicted for both wild-type and mutant channels, with a distance of 2.94 Å and 2.95 Å, respectively (Fig. 8, *D* and *E*, *insets*). On the other hand, a critical difference is apparent in a predicted interaction further down between the pore helix and the SF, involving H^+-bonds between the carbonyl oxygen atom of I312 and nitrogens of both I317 and G318 (Fig. 8, *D* and *E*, *insets*). It is predicted that in the wild-type channel this carbonyl oxygen is not positionally constrained and can thus rotate around its linkage to the α-carbon. However, the presence of the hydroxyl group of a threonine in the 315 position stabilizes the position of this carbonyl via its additional hydrogen bond with the hydroxyl.

We then performed a similar analysis for the A315S and A315V mutants that behaved similarly to A315T and wild-type, respectively. For each, the predicted structures of the SF and associated pore-helix domains are shown superimposed with wild-type (Fig. 9, *A* and *B*, *left*). For both mutants, the distances between the diagonally facing SF carbonyls are predicted to be modestly increased relative to wild-type (Fig. 9, *A* and *B*, *center*). Since their behavior is so opposite, however, this reinforces the conclusion that this structural perturbation is not likely to be the key factor. The networks of H^+-bonding and ''hot-spot'' interactions identified above between the SF and pore helix are shown in Fig. 9, *A* and *B* (*right*). Again, there is no effect of either mutation of the predicted interaction between D321 and W308, with interatomic distances of 2.96 Å and 2.95 Å for A315S and A315V, respectively. However, the stabilization of the position of I317 by the residue at the 315 position is very different, paralleling the difference between wild-type and A315T. Thus, as for A315T, there is a strong H^+-bond between the hydroxyl of S315 and the nitrogen atom of I317, helping to lock the latter in position to maintain H^+-bonding with G318. Conversely, as for A315 (wild-type), there is no such H^+-bond possible between V315 and I317, allowing the I317 carbonyl to torsion out of position, which would prevent H^+-bonding with G318. Thus, we conclude that the critical factor for the 315 position is not hydrophobicity per se, but rather whether it possesses the H^+-donor hydroxyl that enables interactions with I317. Without I317 stabilization, the SF is predicted to be unstable and likely to collapse into a ''nonconducting'' state. We hypothesize that most wild-type and A315V KCNQ3 channels are locked in such a nonfunctional configuration, whereas most of the KCNQ3 A315 and A315S mutants are stabilized in the ''conducting'' state, thus accounting for the dramatically increased expression of *functional* (conducting) channels seen in the latter.

DISCUSSION

In this work, we investigate the mechanisms underlying divergent macroscopic current amplitudes produced by KCNQ channels, with a particular emphasis on KCNQ3 homomers. The issue attains greater importance because of the differential expression of KCNQ1–5 subunits in different neurons of the peripheral and central nervous systems, as well as in the inner ear, heart, and epithelia (60). Given the strong influence of M-channel activity on neuronal discharge properties (61–63) and cellular function in nonneurons, the profoundly divergent currents resulting from the particular KCNQ subunits expressed in a given cell are expected to have far-reaching ramifications. Different neurons in particular have been found to differentially express divergent mixtures of M-type subunits (5,9,10), with distinct subcellular localizations (6,64,65), making it likely that transcriptional control of the family of KCNQ genes is a mechanism for shaping the neuronal response (66). We emphasize that our knowledge of the unitary properties of M channels allows us to convert differences in macroscopic currents into the underlying density of functional channels in the membrane. Thus, whereas the 10-fold differences in whole-cell current between KCNQ3 homomers and KCNQ4 homomers, or KCNQ2/3 heteromers, are already large, simple calculations indicate a difference in the density of functional channels of up to 270-fold (Table 1).

Widely divergent hypotheses have been put forward to explain such divergent expression. Several studies that performed surface luminescence of subunits expressed in oocytes attributed nearly all of the differences in macroscopic currents to differential membrane expression of the channel proteins (19,20,26,29). On the other hand, Etxeberria and colleagues (15) found a poor correlation between current amplitudes and surface expression of various KCNQ2 and KCNQ3 chimeras and point mutants, and concluded that other factors, localized to the transmembrane and N-terminal domains, were responsible. They found that the A315T mutation vastly increases the currents without changing the surface expression of the channels, localizing the effect of the identity of the transmembrane region to the pore structure. Our work here is in full agreement in both aspects. Moreover, we also do not find that the dramatic differences in the density of functional channels can be explained by parallel divergent expression of channels in the membrane. Our TIRF studies

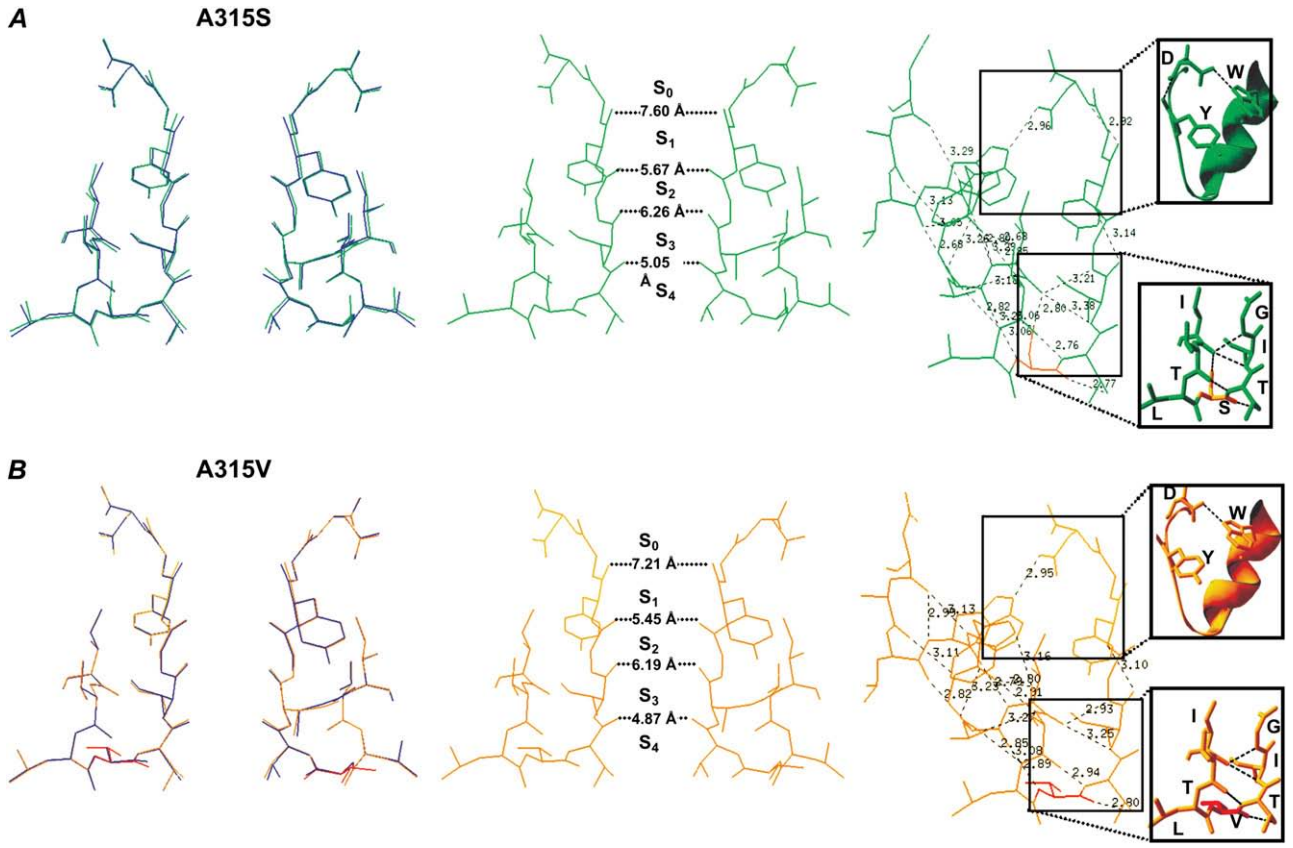

FIGURE 9 The predicted H^+-bonding networks within the pore region of A315S and A315V KCNQ3 mutants are consistent with the stabilization role of a hydroxyl group at residue 315. Shown are the predicted structures and H^+-bonds within and between the pore helix and SF of A315S (*A*) and A315V (*B*) KCNQ3 mutants. The predicted distances (Å) between donor and acceptor for each bond are indicated. In the insets are shown expanded views (rotated by 180°) of the predicted interaction between D321 and W308, and the mini-network of predicted interactions between the GIT of the SF and the pore helix, in the area around S315 (*A*) or V315 (*B*).

did not observe any significant differences of CFP- or YFP-tagged channels in, or very close to, the membrane, and the biotinylation experiments revealed differences that were at most threefold. Thus, two independent measures of surface expression strongly suggest that other mechanisms are dominant.

To our knowledge, all the laboratories are in agreement that the two coiled-coiled domains in the carboxy terminus, contained within the A domain, mediate subunit-specific tetramerization and assembly of functional channels (19,26,67) via the presence of intersubunit salt bridges that are particularly poor in this domain of KCNQ3 but particularly rich for KCNQ4 (27). It has been proposed that these salt-bridge interactions are one control over surface expression (28). We found that the exchange of the KCNQ4 C terminus for that of KCNQ3 in the KCNQ3(TD)Q1 chimera increased the current density by fourfold, consistent with that notion, suggesting that the carboxy-terminal A-domain has this effect independently of the pore-domain control examined in detail in this study. However, restoration of the intersubunit salt-bridge network in KCNQ3 by appropriate mutagenesis did not increase the amplitudes of those currents (27), and the fourfold increase we found by swapping the carboxy-terminus is much too small to account for the 270-fold difference in the calculated density of functional KCNQ3 versus KCNQ4 channels. Thus, we suggest that the coiled-coiled salt-bridge network is permissive for functional tetramers, likely by scaffolding of the subunits together in correct apposition, but that the pore domain structure is the limiting factor.

After close examination, we found that the effect of the TD on the density of functional channels was only modest, with that twofold effect localizing to the same asparagine identified earlier (20), although our TIRF analysis did not detect any difference in the membrane presence of YFP-tagged channels (a caveat is that we cannot exclude a subtle effect of the YFP tag). By far, the major determinant of current density is localized to the intracellular TEA^+ binding site at a location two residues before the SF signature sequence. Replacement of the native alanine in KCNQ3 with a hydroxyl-containing threonine or serine boosted the density of functional channels by more than 25-fold, and the inverse mutation in KCNQ1 reduced it by nearly 15-fold. These changes were not accompanied by any significant changes in membrane abundance detected by TIRF microscopy, leading us to consider structural hypotheses. The Ba^{2+} block data

strengthen that consideration. Two lines of investigation in this respect seem to be most germane to our thinking here. The first is documented by a large literature suggesting that the SF of K^+ channels is intrinsically unstable in the absence of extrinsic stabilizing forces, and that the pore can exist in ''conducting'' and ''nonconducting'' conformations, linked to permeating ions. Early work indicated that removal of permeant ions led to K^+ channels becoming nonfunctional (68). The mechanism of this experimental result has been shown structurally to be the alternative conformation of the SF in conductive and collapsed conformations induced by the presence of either low, or physiological, concentrations of K^+ (52,53,57). Thus, in addition to the helix bundle crossing that likely forms the main voltage-dependent gate of Kv channels (69–71), conformational rearrangements of the SF represent another gate, underlying phenomena such as C-type inactivation (43). However, two well-established tests for a C-type inactivation mechanism underlying a putative nonconducting conformation of KCNQ3 channels were negative, and even during very long recordings we did not detect any inactivation of KCNQ3-containing channels. Moreover, the mutations at the 315 position that dramatically affected current amplitudes were not accompanied by structural models indicating overt changes in intersubunit carbonyl distances that would be expected by a ''pinching off'' of the permeation pathway.

The second line of inquiry has used crystallographic analysis to suggest that the pore of K^+ channels can exist in alternate conformations with dramatically different gating characteristics (54,55). Thus, the x-ray structure of the E71A mutant of KcsA may adopt not one but two structures, differing in whether the D80 side-chain is ''flipped'' up by 8 Å, and whether W67 adopts one of two possible rotamers. One interpretation of those data suggests that the ''flipped'' and ''nonflipped'' configurations correlate with the very different steady-state open probabilities exhibited by the wild-type and E71A channels (although this is not proved). Our homology modeling does not have the capability to take molecular ''snapshots'' of the channel in different possible conformations, as is possible with actual crystal structures. Moreover, since our models are subjected to energy minimization, we cannot know whether the final model produced is stable or is only a conformation that, although it is most energetically favorable, is not the predominant conformation of that particular protein. The modeling does suggest, however, that the carbonyl of I312 is free to rotate, and that the critical bonds it is predicted to make with SF residues are consequently unstable. Thus, we suggest that the functional KCNQ3 channels that produce currents are those residing in the minority structural conformation represented by the homology model, whereas the more frequent nonconducting conformations are electrically silent yet detected on the surface by the biotinylation and TIRF microscopy assays. However, the critical importance shown by the Perozo lab (54,55) for the stability of the KcsA SF of the H^+-bond between D80 and W67, and the carboxy-carboxylate interaction between D80 and E71 do not seem to be key factors here, since the predicted interactions between D321 and W308 of KCNQ3 are predicted to be nearly identical for the wild-type channel and all the mutants.

Recently, the Attali lab described a slow inactivation mechanism localized to the SF of KCNQ1, induced by the Leu-Phe mutation of residue 273 in S_5 (48). Like the mechanism proposed here, high external [K^+] did not relieve that inactivation, ruling out a C-type inactivation process. A major tool in that study was the use of Ba^{2+} ions as a structural probe of the channel pore, correlating Ba^{2+} block with structural alterations of the SF induced by mutations. Although we only briefly studied Ba^{2+} block in this work, we also predict a similar structural correspondence. Gibon and colleagues also successfully used homology modeling, using the solved structure of Kv1.2 as a template, to show that the L273F mutation causes a decrease in the flexibility of the SF at the level of the S_1 permeant ion binding site, mediating their inactivation process seen experimentally (48). In our structural homology model, we did not observe any large differences in the distance between diagonally facing carbonyls in the SF that correlated with the density of functional channels. For instance, the A315T mutation increased the predicted distance between opposing G318 carbonyls, and A315S even more so, but although that distance for the A315V mutant is also predicted to be significantly larger than for the wild-type, the currents from A315V were tiny. Thus, our proposed mechanism does not involve differences in intersubunit carbonyl spacing, although we cannot rule out effects on SF flexibility.

What our modeling does indicate is the potentially critical stabilizing role of the residue at the 315 position in stabilizing the position of the carbonyl of I312. KCNQ3 is unique among KCNQ channels, and almost all other K^+ channels, in not having the hydrophilic threonine at that position. The carbonyl of I312 is involved in H^+-bonds with both G320 and I321; thus, if the I312 carbonyl adopts a torsional position out of range for those stabilizing interactions, the SF would likely collapse at the S_3 and S_4 permeant ion sites. This hypothesis is similar to the effect of the T75 mutation in KcsA (T316 in KCNQ3), which was shown by crystallographic analysis to cause a destabilization of the lower SF at site S_4 (73). What is clear from many studies is that alterations in structure more than 10–20 Å away can alter the stability of the SF, whose conductive conformations are being appreciated as not static, but rather fluid in nature (54,73,74). Here, the hypothesized critical interactions are much closer ($<$3 Å). We suggest that, unique among KCNQ channels, most wild-type KCNQ3 channels adopt a ''structurally-locked'' conformation in which the assembled channel tetramers are in the membrane with an abundance similar to the other KCNQ channels, but are functionally dormant. Mutation of the A315 to a hydroxyl-containing residue, such as a threonine or a serine, prevents the SF structure from locking closed, and enables large macroscopic currents of

similar magnitude to KCNQ2/3 heteromers or KCNQ1 and KCNQ4 homomers. We look forward to the crystal structures of M-type channels being solved, so that we can directly observe the structural conformations corresponding to gating of the channels, and to the conformations that may underlie the functionality or dormancy of such channels that can adopt nonconductive arrangement of their pores.

SUPPLEMENTARY MATERIAL

To view all of the supplemental files associated with this article, visit www.biophysj.org.

We thank Pamela Martin and Sara Kathryn Boyd for expert technical assistance, Michael Schwake for the KCNQ3/(TD)KCNQ1 chimera, and Brad Rothberg for helpful discussions.

This work was supported by American Heart Association (Texas Affiliate) research award 0755071Y and by National Institutes of Health grant NS43394 to M.S.S.

REFERENCES

1. Robbins, J. 2001. KCNQ potassium channels: physiology, pathophysiology, and pharmacology. *Pharmacol. Ther.* 90:1–19.
2. Delmas, P., and D. A. Brown. 2005. Pathways modulating neural KCNQ/M (Kv7) potassium channels. *Nat. Rev. Neurosci.* 6:850–862.
3. Jespersen, T., M. Grunnet, and S. P. Olesen. 2005. The KCNQ1 potassium channel: from gene to physiological function. *Physiology (Bethesda).* 20:408–416.
4. Wang, H. S., Z. Pan, W. Shi, B. S. Brown, R. S. Wymore, I. S. Cohen, J. E. Dixon, and D. McKinnon. 1998. KCNQ2 and KCNQ3 potassium channel subunits: molecular correlates of the M-channel. *Science.* 282:1890–1893.
5. Cooper, E. C., E. Harrington, Y. N. Jan, and L. Y. Jan. 2001. M channel KCNQ2 subunits are localized to key sites for control of neuronal network oscillations and synchronization in mouse brain. *J. Neurosci.* 21:9529–9540.
6. Devaux, J. J., K. A. Kleopa, E. C. Cooper, and S. S. Scherer. 2004. KCNQ2 is a nodal K^+ channel. *J. Neurosci.* 24:1236–1244.
7. Cooper, E. C., K. D. Aldape, A. Abosch, N. M. Barbaro, M. S. Berger, W. S. Peacock, Y. N. Jan, and L. Y. Jan. 2000. Colocalization and coassembly of two human brain M-type potassium channel subunits that are mutated in epilepsy. *Proc. Natl. Acad. Sci. USA.* 97:4914–4919.
8. Passmore, G. M., A. A. Selyanko, M. Mistry, M. Al-Qatari, S. J. Marsh, E. A. Matthews, A. H. Dickenson, T. A. Brown, S. A. Burbidge, M. Main, and D. A. Brown. 2003. KCNQ/M currents in sensory neurons: significance for pain therapy. *J. Neurosci.* 23:7227–7236.
9. Lerche, C., C. R. Scherer, G. Seebohm, C. Derst, A. D. Wei, A. E. Busch, and K. Steinmeyer. 2000. Molecular cloning and functional expression of KCNQ5, a potassium channel subunit that may contribute to neuronal M-current diversity. *J. Biol. Chem.* 275:22395–22400.
10. Schroeder, B. C., M. Hechenberger, F. Weinreich, C. Kubisch, and T. J. Jentsch. 2000. KCNQ5, a novel potassium channel broadly expressed in brain, mediates M-type currents. *J. Biol. Chem.* 275: 24089–24095.
11. Shah, M. M., M. Mistry, S. J. Marsh, D. A. Brown, and P. Delmas. 2002. Molecular correlates of the M-current in cultured rat hippocampal neurons. *J. Physiol.* 544:29–37.
12. Yus-Najera, E., A. Munoz, N. Salvador, B. S. Jensen, H. B. Rasmussen, J. Defelipe, and A. Villarroel. 2003. Localization of KCNQ5 in the normal and epileptic human temporal neocortex and hippocampal formation. *Neuroscience.* 120:353–364.
13. Coucke, P. J., P. V. Hauwe, P. M. Kelley, H. Kunst, I. Schatteman, D. V. Velzen, J. Meyers, R. J. Ensink, M. Verstreken, F. Declau, H. Marres, K. Kastury, S. Bhasin, W. T. McGuirt, R. J. Smith, C. W. Cremers, P. V. Heyning, P. J. Willems, S. D. Smith, and G. V. Camp. 1999. Mutations in the KCNQ4 gene are responsible for autosomal dominant deafness in four DFNA2 families. *Hum. Mol. Genet.* 8:1321–1328.
14. Kubisch, C., B. C. Schroeder, T. Friedrich, B. Lutjohann, A. El-Amraoui, S. Marlin, C. Petit, and T. J. Jentsch. 1999. KCNQ4, a novel potassium channel expressed in sensory outer hair cells, is mutated in dominant deafness. *Cell.* 96:437–446.
15. Etxeberria, A., I. Santana-Castro, M. P. Regalado, P. Aivar, and A. Villarroel. 2004. Three mechanisms underlie KCNQ2/3 heteromeric potassium M-channel potentiation. *J. Neurosci.* 24:9146–9152.
16. Schroeder, B. C., C. Kubisch, V. Stein, and T. J. Jentsch. 1998. Moderate loss of function of cyclic-AMP-modulated KCNQ2/KCNQ3 K^+ channels causes epilepsy. *Nature.* 396:687–690.
17. Yang, W. P., P. C. Levesque, W. A. Little, M. L. Conder, P. Ramakrishnan, M. G. Neubauer, and M. A. Blanar. 1998. Functional expression of two KvLQT1-related potassium channels responsible for an inherited idiopathic epilepsy. *J. Biol. Chem.* 273:19419–19423.
18. Gamper, N., J. D. Stockand, and M. S. Shapiro. 2003. Subunit-specific modulation of KCNQ potassium channels by Src tyrosine kinase. *J. Neurosci.* 23:84–95.
19. Schwake, M., D. Athanasiadu, C. Beimgraben, J. Blanz, C. Beck, T. J. Jentsch, P. Saftig, and T. Friedrich. 2006. Structural determinants of M-type KCNQ (Kv7) K^+ channel assembly. *J. Neurosci.* 26:3757–3766.
20. Schenzer, A., T. Friedrich, M. Pusch, P. Saftig, T. J. Jentsch, J. Grotzinger, and M. Schwake. 2005. Molecular determinants of KCNQ (Kv7) K^+ channel sensitivity to the anticonvulsant retigabine. *J. Neurosci.* 25:5051–5060.
21. Gamper, N., Y. Li, and M. S. Shapiro. 2005. Structural requirements for differential sensitivity of KCNQ K^+ channels to modulation by Ca^{2+}/calmodulin. *Mol. Biol. Cell.* 16:3538–3551.
22. Li, Y., N. Gamper, and M. S. Shapiro. 2004. Single-channel analysis of KCNQ K^+ channels reveals the mechanism of augmentation by a cysteine-modifying reagent. *J. Neurosci.* 24:5079–5090.
23. Selyanko, A. A., J. K. Hadley, and D. A. Brown. 2001. Properties of single M-type KCNQ2/KCNQ3 potassium channels expressed in mammalian cells. *J. Physiol.* 534:15–24.
24. Pusch, M. 1998. Increase of the single-channel conductance of KvLQT1 potassium channels induced by the association with minK. *Pflugers Arch.* 437:172–174.
25. Li, Y., N. Gamper, D. W. Hilgemann, and M. S. Shapiro. 2005. Regulation of Kv7 (KCNQ) K^+ channel open probability by phosphatidylinositol (4,5)-bisphosphate. *J. Neurosci.* 25:9825–9835.
26. Schwake, M., T. J. Jentsch, and T. Friedrich. 2003. A carboxy-terminal domain determines the subunit specificity of KCNQ K^+ channel assembly. *EMBO Rep.* 4:76–81.
27. Howard, R. J., K. A. Clark, J. M. Holton, and D. L. Minor, Jr. 2007. Structural insight into KCNQ (Kv7) channel assembly and channelopathy. *Neuron.* 53:663–675.
28. Nakajo, K., and Y. Kubo. 2008. Second coiled-coil domain of KCNQ channel controls current expression and subfamily specific heteromultimerization by salt bridge networks. *J. Physiol.* 586:2827–2840.
29. Schwake, M., M. Pusch, T. Kharkovets, and T. J. Jentsch. 2000. Surface expression and single channel properties of KCNQ2/KCNQ3, M-type K^+ channels involved in epilepsy. *J. Biol. Chem.* 275:13343–13348.
30. Gamper, N., J. D. Stockand, and M. S. Shapiro. 2005. The use of Chinese hamster ovary (CHO) cells in the study of ion channels. *J. Pharmacol. Toxicol. Methods.* 51:177–185.
31. Axelrod, D. 2003. Total internal reflection fluorescence microscopy in cell biology. *Methods Enzymol.* 361:1–33.
32. Rae, J., K. Cooper, P. Gates, and M. Watsky. 1991. Low access resistance perforated patch recordings using amphotericin B. *J. Neurosci. Methods.* 37:15–26.

33. Jiang, Y., A. Lee, J. Chen, V. Ruta, M. Cadene, B. T. Chait, and R. MacKinnon. 2003. X-ray structure of a voltage-dependent K^+ channel. *Nature*. 423:33–41.
34. Schwede, T., J. Kopp, N. Guex, and M. C. Peitsch. 2003. SWISS-MODEL: an automated protein homology-modeling server. *Nucleic Acids Res*. 31:3381–3385.
35. Axelrod, D., T. P. Burghardt, and N. L. Thompson. 1984. Total internal reflection fluorescence. *Annu. Rev. Biophys. Bioeng*. 13:247–268.
36. Steyer, J. A., and W. Almers. 2001. A real-time view of life within 100 nm of the plasma membrane. *Nat. Rev. Mol. Cell Biol*. 2:268–275.
37. Tong, Q., N. Gamper, J. L. Medina, M. S. Shapiro, and J. D. Stockand. 2004. Direct activation of the epithelial Na^+ channel by phosphatidylinositol 3,4,5-trisphosphate and phosphatidylinositol 3,4-bisphosphate produced by phosphoinositide 3-OH kinase. *J. Biol. Chem*. 279:22654–22663.
38. Bal, M., O. Zaika, P. Martin, and M. S. Shapiro. 2008. Calmodulin binding to M-type K^+ channels assayed by TIRF/FRET in living cells. *J. Physiol*. 586:2307–2320.
39. Doyle, D. A., J. Morais Cabral, R. A. Pfuetzner, A. Kuo, J. M. Gulbis, S. L. Cohen, B. T. Chait, and R. MacKinnon. 1998. The structure of the potassium channel: molecular basis of K^+ conduction and selectivity. *Science*. 280:69–77.
40. MacKinnon, R., and C. Miller. 1989. Mutant potassium channels with altered binding of charybdotoxin, a pore-blocking peptide inhibitor. *Science*. 245:1382–1385.
41. MacKinnon, R., L. Heginbotham, and T. Abramson. 1990. Mapping the receptor site for charybdotoxin, a pore-blocking potassium channel inhibitor. *Neuron*. 5:767–771.
42. Yus-Najera, E., I. Santana-Castro, and A. Villarroel. 2002. The identification and characterization of a noncontinuous calmodulin binding site in non-inactivating voltage-dependent KCNQ potassium channels. *J. Biol. Chem*. 277:28545–28553.
43. Yellen, G. 1998. The moving parts of voltage-gated ion channels. *Q. Rev. Biophys*. 31:239–295.
44. Lopez-Barneo, J., T. Hoshi, S. H. Heinemann, and R. W. Aldrich. 1993. Effects of external cations and mutations in the pore region on C-type inactivation of *Shaker* potassium channels. *Receptors Channels*. 1:61–71.
45. Armstrong, C. M., R. P. Swenson, Jr., and S. R. Taylor. 1982. Block of squid axon K^+ channels by internally and externally applied barium ions. *J. Gen. Physiol*. 80:663–682.
46. Robbins, J., J. Trouslard, S. J. Marsh, and D. A. Brown. 1992. Kinetic and pharmacological properties of the M-current in rodent neuroblastoma × glioma hybrid cells. *J. Physiol*. 451:159–185.
47. Gibor, G., D. Yakubovich, A. Peretz, and B. Attali. 2004. External barium affects the gating of KCNQ1 potassium channels and produces a pore block via two discrete sites. *J. Gen. Physiol*. 124:83–102.
48. Gibor, G., D. Yakubovich, A. Rosenhouse-Dantsker, A. Peretz, H. Schottelndreier, G. Seebohm, N. Dascal, D. E. Logothetis, Y. Paas, and B. Attali. 2007. An inactivation gate in the selectivity filter of KCNQ1 potassium channels. *Biophys. J*. 93:4159–4172.
49. Neyton, J., and C. Miller. 1988. Discrete Ba^{2+} block as a probe of ion occupancy and pore structure in the high-conductance Ca^{2+}-activated K^+ channel. *J. Gen. Physiol*. 92:569–586.
50. Neyton, J., and C. Miller. 1988. Potassium blocks barium permeation through a calcium-activated potassium channel. *J. Gen. Physiol*. 92:549–567.
51. Jiang, Y., and R. MacKinnon. 2000. The barium site in a potassium channel by x-ray crystallography. *J. Gen. Physiol*. 115:269–272.
52. Lockless, S. W., M. Zhou, and R. MacKinnon. 2007. Structural and thermodynamic properties of selective ion binding in a K^+ channel. *PLoS Biol*. 5:e121.
53. Valiyaveetil, F. I., M. Leonetti, T. W. Muir, and R. Mackinnon. 2006. Ion selectivity in a semisynthetic K^+ channel locked in the conductive conformation. *Science*. 314:1004–1007.
54. Cordero-Morales, J. F., L. G. Cuello, Y. Zhao, V. Jogini, D. M. Cortes, B. Roux, and E. Perozo. 2006. Molecular determinants of gating at the potassium-channel selectivity filter. *Nat. Struct. Mol. Biol*. 13:311–318.
55. Cordero-Morales, J. F., V. Jogini, A. Lewis, V. Vasquez, D. M. Cortes, B. Roux, and E. Perozo. 2007. Molecular driving forces determining potassium channel slow inactivation. *Nat. Struct. Mol. Biol*. 14:1062–1069.
56. Zhou, Y., and R. MacKinnon. 2003. The occupancy of ions in the K^+ selectivity filter: charge balance and coupling of ion binding to a protein conformational change underlie high conduction rates. *J. Mol. Biol*. 333:965–975.
57. Zhou, Y., J. H. Morais-Cabral, A. Kaufman, and R. MacKinnon. 2001. Chemistry of ion coordination and hydration revealed by a K^+ channel-Fab complex at 2.0 A resolution. *Nature*. 414:43–48.
58. Liu, Y., M. E. Jurman, and G. Yellen. 1996. Dynamic rearrangement of the outer mouth of a K^+ channel during gating. *Neuron*. 16:859–867.
59. Yellen, G., D. Sodickson, T. Y. Chen, and M. E. Jurman. 1994. An engineered cysteine in the external mouth of a K^+ channel allows inactivation to be modulated by metal binding. *Biophys. J*. 66:1068–1075.
60. Brown, D. A. 2008. Kv7 (KCNQ) potassium channels that are mutated in human diseases. *J. Physiol*. 586:1781–1783.
61. Yue, C., and Y. Yaari. 2006. Axo-somatic and apical dendritic Kv7/M channels differentially regulate the intrinsic excitability of adult rat CA1 pyramidal cells. *J. Neurophysiol*. 95:3480–3495.
62. Peretz, A., A. Sheinin, C. Yue, N. Degani-Katzav, G. Gibor, R. Nachman, A. Gopin, E. Tam, D. Shabat, Y. Yaari, and B. Attali. 2007. Pre- and postsynaptic activation of M-channels by a novel opener dampens neuronal firing and transmitter release. *J. Neurophysiol*. 97:283–295.
63. Maljevic, S., T. V. Wuttke, and H. Lerche. 2008. Nervous system Kv7 disorders: breakdown of a subthreshold brake. *J. Physiol*. 586:1791–1801.
64. Pan, Z., T. Kao, Z. Horvath, J. Lemos, J. Y. Sul, S. D. Cranstoun, V. Bennett, S. S. Scherer, and E. C. Cooper. 2006. A common ankyrin-G-based mechanism retains KCNQ and NaV channels at electrically active domains of the axon. *J. Neurosci*. 26:2599–2613.
65. Chung, H. J., Y. N. Jan, and L. Y. Jan. 2006. Polarized axonal surface expression of neuronal KCNQ channels is mediated by multiple signals in the KCNQ2 and KCNQ3 C-terminal domains. *Proc. Natl. Acad. Sci. USA*. 103:8870–8875.
66. Saganich, M. J., E. Machado, and B. Rudy. 2001. Differential expression of genes encoding subthreshold-operating voltage-gated K^+ channels in brain. *J. Neurosci*. 21:4609–4624.
67. Maljevic, S., C. Lerche, G. Seebohm, A. K. Alekov, A. E. Busch, and H. Lerche. 2003. C-terminal interaction of KCNQ2 and KCNQ3 K^+ channels. *J. Physiol*. 548:353–360.
68. Almers, W., and C. M. Armstrong. 1980. Survival of K^+ permeability and gating currents in squid axons perfused with K^+-free media. *J. Gen. Physiol*. 75:61–78.
69. Perozo, E., D. M. Cortes, and L. G. Cuello. 1999. Structural rearrangements underlying K^+-channel activation gating. *Science*. 285: 73–78.
70. del Camino, D., and G. Yellen. 2001. Tight steric closure at the intracellular activation gate of a voltage-gated K^+ channel. *Neuron*. 32:649–656.
71. Jiang, Y., A. Lee, J. Chen, M. Cadene, B. T. Chait, and R. MacKinnon. 2002. Crystal structure and mechanism of a calcium-gated potassium channel. *Nature*. 417:515–522.
72. Long, S. B., E. B. Campbell, and R. Mackinnon. 2005. Crystal structure of a mammalian voltage-dependent *Shaker* family K^+ channel. *Science*. 309:897–903.
73. Zhou, M., and R. MacKinnon. 2004. A mutant KcsA K^+ channel with altered conduction properties and selectivity filter ion distribution. *J. Mol. Biol*. 338:839–846.
74. Berneche, S., and B. Roux. 2005. A gate in the selectivity filter of potassium channels. *Structure*. 13:591–600.